Mathematical Modelling of Sticking Phenomena in COREX Reduction Shaft by CFD-DEM Method

Author:
Samman, Mohammed

Publication Date:
2015

DOI:
https://doi.org/10.26190/unsworks/18190

Mathematical Modelling of Sticking Phenomena in COREX Reduction Shaft by CFD-DEM Method

By

Mohammed Essa Samman

A thesis submitted in fulfilment

of the requirements for the degree of

Master of Philosophy (Research)

Laboratory for Simulation and Modelling of Particulate Systems

School of Materials Science and Engineering

Faculty of Science

The University of New South Wales

March 2015

ORIGINALITY STATEMENT

'I hereby declare that this submission is my own work and to the best of my knowledge it contains no materials previously published or written by another person, or substantial proportions of material which have been accepted for the award of any other degree or diploma at UNSW or any other educational institution, except where due acknowledgement is made in the thesis. Any contribution made to the research by others, with whom I have worked at UNSW or elsewhere, is explicitly acknowledged in the thesis. I also declare that the intellectual content of this thesis is the product of my own work, except to the extent that assistance from others in the project's design and conception or in style, presentation and linguistic expression is acknowledged.'

Signed …… 

Date ……19/05/2015

ABSTRACT

Liquid iron for steel production is produced mainly in a conventional blast furnace (BF). New iron-making processes have been introduced in the last two decades because of environmental concerns. One such process is COREX smelting technology, which can operate, at least in theory, without any need for coking-coal, significantly reducing CO_2 emissions and production costs of liquid iron. However, the complicated gas-solid flow inside the reduction shaft (RS) of COREX gives rise to operational difficulties such as sticking of particles at high temperature. Understanding the flow patterns in RS would enhance the ability to control them, resulting in an improved overall process quality. To understand multiphase flow in the RS, mathematical modelling has been employed here, coupling discrete element method (DEM) with computational fluid dynamics (CFD). Using this CFD-DEM approach, gas-solid flow and heat transfer phenomena were investigated at microscopic level. The results indicate that gas inlet velocity has an insignificant effect on solid flow pattern due to small gas-solid interaction forces. The model was able to describe heat transfer inside the RS, and a new burden distribution arrangement was proposed, with some improvement in heat transfer in the central part of the furnace. While future analysis and investigation should deal with more realistic properties, these results confirm that mathematical modelling, in particular CFD-DEM, is an effective tool for describing complicated phenomena inside the RS. The findings of this study should be useful for control and optimization of the RS operation.

Keywords: COREX; reduction shaft; multiphase flow; sticking; discrete element method; computational fluid dynamics.

ACKNOWLEDGMENT

I would like to express my gratitude to my wife for her patience and support over the whole period of study, and during all the ups and downs, as well as to my beautiful daughter, Aljori.

My thank and appreciation goes out to my supervisor, Dr Ruiping Zou, and to my co-supervisors, Professor Aibing Yu and Dr Qinfu Hou, for their limitless support and guidance.

Special thanks and gratitude to SABIC and their management for offering me the scholarship, and for their support before and during the study; this Master degree would not have been possible without their support.

Finally but importantly, I am totally grateful to my parents, who passed away a few years ago, for their limitless and boundless support and love. I dedicate this work for their souls.

TABLE OF CONTENTS

LIST OF FIGURES

LIST OF TABLES

Chapter 1 INTRODUCTION

1.1 Preface

Until very recently, iron for steel production has mainly been produced in a conventional blast furnace (BF). However, BF operation is associated with a range of environmental concerns that include CO_2 emission from the process itself as well as from the processing and transport of iron ore, coke and limestone. Additionally, the price of coke has increased dramatically in recent years, further contributing to the urgent need to address these issues by developing new processes. New technologies have been introduced with good potential to replace these processes, or at least to play an important role in the iron-making industry. One such smelting technology is the COREX/FINEX process. Developed by SIEMENS VAI and DVAI-Germany in 1985, COREX is the first commercially proven smelting reduction technology.

The most innovative feature of the COREX process is the separation of the iron reduction and smelting into two separate reactors: reduction shaft (RS) and melter-gasifier. As shown in Figure 1.1, the RS is located exactly over the melter-gasifier, minimizing the space utilized and so reducing the cost of product handling. Moreover, the process is capable of using non-coking coal as a reducing agent and energy source (Chatterjee, 2005), and the system export gas has a wide range of applications (Wall et al., 2011). Although this process was introduced to overcome the problems associated with coke consumption, coke is still used in most COREX plants worldwide. To that extent, COREX still has some drawbacks, such as high consumption of coal (more than that of a BF), the difficulty of efficiently distributing Direct Reduced Iron (DRI) and coal in the melter-gasifier and the segregation and sticking of particles inside the system. In the present study, these sticking phenomena will be investigated, particularly in the RS of the COREX process.

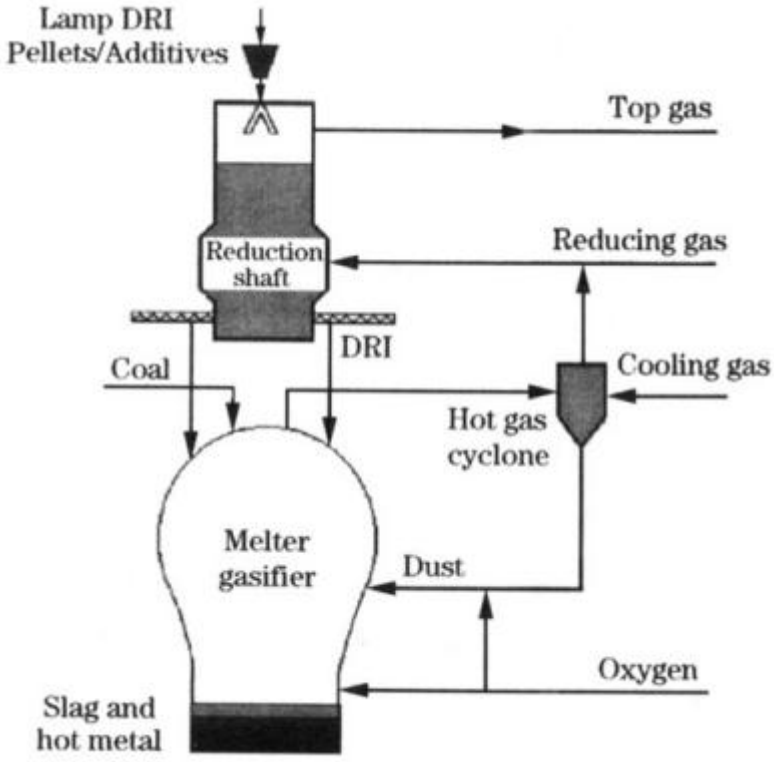

Figure 1.1: Simple illustration of COREX process (Barman et al., 2011).

The first COREX commercial plant was commissioned in Pretoria, South Africa in 1989, with an annual capacity of 315,000 tons of pig iron. Today, annual production from the seven COREX plants currently operating exceeds 8 million tons of pig iron. These plants are located in South Africa, China and India (Siemens VAI, 2011).

The process starts by charging iron ores, pellets or lumps and flux materials into the RS to produce DRI by exposure to counter-current reducing gases. DRI usually reaches up to 93–95% metallization and contains 2–5 wt% carbon. Residence time inside the furnace is about 7–9 hours (Anameric and Kawatra, 2008), which is a long time by comparison with other DRI processes such as Midrex or Tenova HYL. Discharge screws convey the DRI into the melter-gasifier, where final reduction takes place along with other metallurgical reactions. Hot metal and slag is then tapped as in the conventional BF process. The coal is injected directly into the melter-gasifier and

gasified by oxygen injection, producing high efficient reduction gases. The gas produced mostly contains carbon monoxide (CO = 65–70%), hydrogen (H_2 = 20–25%) and carbon dioxide (CO_2 = 2–4%) (Anameric and Kawatra, 2008). These gases leave the melter-gasifier and are cleaned and cooled to about 800 °C and then injected into the RS (bustle zone), reducing iron ores to DRI. The off-gases produced by the system have high calorific values of about 6.7–8.0 MJ/nm^3, containing 35–45% CO, 35–45% CO_2, 15–20% H_2, 1–3% N_2 and 1–4% CH_4 (Wingrove, 1999). These gases can be used for various purposes such as generating electricity, reducing ores in adjacent direct reduction plants and for preheating purposes inside plants. The economic efficiency of the COREX process depends strongly on the beneficiation of these gases.

The quality of DRI (i.e. metallization) is an important element. This can generally be managed by controlling factors such as amount and quality of reducing gases (especially %CO and %H_2), temperature of the reduction gas, reducibility of the iron ores, average particle size and distribution of the solids charged. On the other hand, the efficiency of the melter-gasifier has been found to depend on the size and chemical analysis of the coal used, as well as on the high percentage of H_2 and CO in the reducing gas to ensure high metallization of the DRI, optimum distribution of oxygen between tuyeres and dust burners, permeability of the char bed, high system pressure and a large melting operation (i.e. large amounts of hot metal produced per hour). In the next section, the RS will be discussed in more detail.

1.2 Reduction Shaft (RS)

The COREX RS is a tube-like reactor that utilizes the same principle as well-known direct reduction processes like Midrex and Tenova HYL. Direct reduction is the process of converting iron ore into metallic iron (spongy iron) by using reductant gases

such as H_2 and CO in gas-based reduction, or coal in coal-based reduction processes. In recent years, the demand for DRI has increased as an alternative to high quality scrap. In advanced countries, electric arc furnace (EAF) mills now are predominant in the steel industry, boosting the demand for DRI. Figure 1.2 shows the share of each process in DRI production from 2009 to 2011 (Midrex Technologies, 2014).

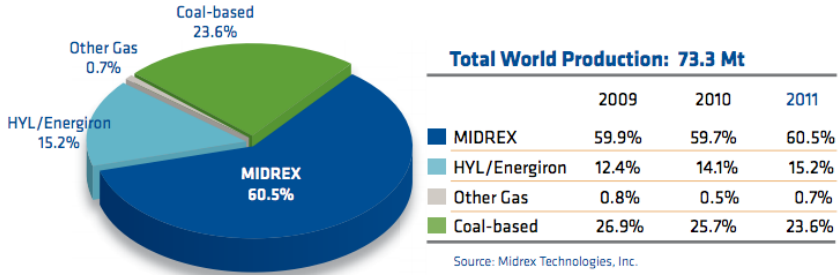

Figure 1.2: Share of each process in DRI production (with annual increases) (Midrex Technologies, 2014).

The iron reduction mechanism is simple; fresh iron ores are exposed in a reactor or the RS to reductant gases or coal at high temperature (usually in the range of 750–1050 °C) to reduce (extract) oxygen from the iron and introduce metallic iron (DRI). The reactions converting Hematite (Fe_2O_3) into metallic iron (Fe) are listed below.

- Reactions with H_2:

$$3Fe_2O_3 + H_2 = 2Fe_3O_4 + H_2O \quad (1.1)$$

$$Fe_3O_4 + H_2 = 3FeO + H_2O \quad (1.2)$$

$$FeO + H_2 = Fe + H_2O \quad (1.3)$$

- Reactions with CO:

$$3Fe_2O_3 + CO = 2Fe_3O_4 + CO_2 \quad (1.4)$$

$$Fe_3O_4 + CO = 3FeO + CO_2 \quad (1.5)$$

$$FeO + CO = Fe + CO_2 \quad (1.6)$$

The most widely-known DRI production technologies are the MIDREX® and Tenova HYL® processes. The first Midrex plant was commissioned at Portland, Oregon USA in 1969; by 2017, the company expects to produce a cumulative one billion tons of DRI (Midrex Technologies, 2014). The second largest producer of DRI is Tenova HYL; the Mexican company HYL was established in 1957. Many of these processing facilities have been built in developing countries, particularly those producing natural gas.

In all direct reduction furnaces, the two most common issues are segregation and sticking of feed materials. Segregation is introduced in a RS as a consequence of natural size distribution among ore particles or between ore and coal particles. Many previous studies have investigated the root cause of this issue (e.g. (Alavi Shoushtari et al., 2013, Drahun and Bridgwater, 1983, Gernon and Gilbertson, 2012, Rahman et al., 2011, Standish, 1985, Williams, 1976). Although most studies have concentrated on other particulate systems such as hopper or fluidization systems, an understanding of solid flow in the COREX reduction shaft is of great importance as the first step in achieving a smooth operation. In COREX, most of the feed materials are large in size, but the introduction of fines during the transportation and processing of iron ores and coal is also possible. In association with injected reducing gases, these fines may have significant effects on both segregation and sticking. High temperatures, along with the physical and chemical properties of iron ores, also have a crucial effect on either increasing or minimizing the sticking. In the following sections, an attempt will be made to understand the phenomenon of sticking.

1.3 Aim of the Project

Although COREX is a promising new process, there is to date relatively little

significant research relating specifically to its first component, the RS. From related experience with the Midrex RS and on the basis of this literature survey, it becomes clear that sticking and segregation of solid particles are the major two problems facing the direct reduction industry. An understanding of these issues will therefore contribute significantly to smooth operation and increased productivity. The literature indicates that CFD-DEM mathematical simulation can generate detailed particle-scale information, for instance, about the trajectories of individual particles and the forces acting on them (Yu, 2004), enabling interpretation of the mechanisms governing complicated flow behaviours like sticking or segregation. On that basis, the CFD-DEM method has proved to be an effective approach to simulate a COREX RS (Hou et al., 2014).

The present study will apply the CFD-DEM approach to further fundamental understanding of sticking phenomena, which should be useful for process control and optimization. The specific research objectives are to investigate:

1. Gas-solid flow inside the RS, using the CFD-DEM model
2. Effect of gas flow on solid movement
3. Heat transfer characteristics in the RS
4. Effect of burden distribution

Chapter 2 LITERATURE REVIEW

2.1 Effects of Cohesive Force on Solid-fluid Flow inside the Reduction Shaft

For large particles, effective weight dominates flow behaviour. Effective particle weight decreases with decreasing particle size while the ratio of cohesive force between particles to particle weight increases, and therefore, the cohesive force finally becomes the key factor in controlling flow behaviour. COREX RS feedstock commonly contains different types and sizes of raw materials: ores, coals and coal dust. These differences increase the segregation of particles owing to percolation or sifting phenomena, in which smaller particles will move down through the centre of the moving bed, and larger ones will descend near the furnace wall. Following this uneven distribution of particles, the bed's permeability will vary; areas of high permeability (larger particles) will achieve better gas-solid interaction, leading to variations of quality in DRI production.

From the point of view of cohesion, a high cohesion occurs when particles are so small as to exist in powder form. These tend to stick together, forming an agglomerate and leading to harsh effects on solid flow. The following are some brief examples of these forces.

(a) Capillary forces

Liquid bridges formed between particles induce capillary forces. Total capillary force is the sum of surface tension force and force created by the pressure difference across the air-liquid interface. Depending on the amount of liquid added to the system, there are four degrees of saturation: pendular, funicular, capillary and droplet (Figure 2.1). In the pendular regime, all liquid bridges are separate and independent, and the attractive forces between particles are larger as compared to those in the other three regimes. With the addition of more liquid to the system, the degree of saturation of the

system changes—first to funicular, then to capillary and finally reaching the droplet state. The effect of capillary forces was excluded because no liquid is introduced in normal RS operation. However, this force might become effective if particles reached their melting point.

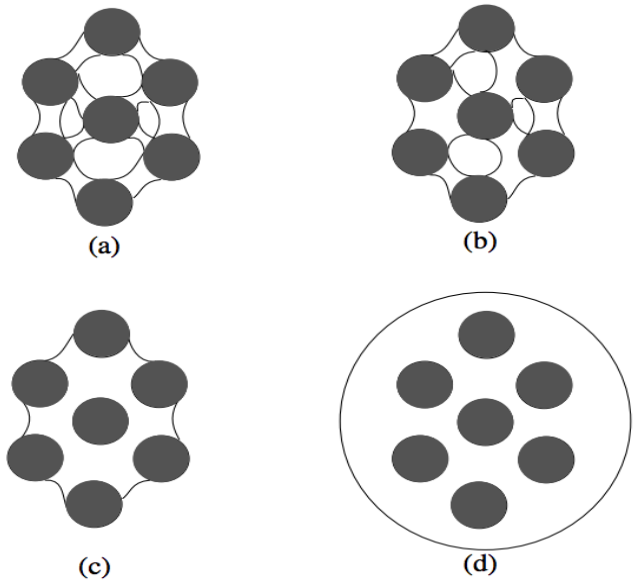

Figure 2.1: Degree of liquid saturation: (a) pendular; (b) funicular; (c) capillary; (d) droplet (Payam and Fathipour, 2011).

(b) Electrostatic forces

Electrostatic forces can be introduced through friction, leading to electrostatic charging of particles by the transfer of electrons between them. One simple instance of this force occurs when a small balloon is rubbed with wool cloth.

(c) Van der Waals force

This is a short-range force, acting when surfaces are sufficiently close together and caused by spontaneous electrical and magnetic polarizations that create a fluctuating electromagnetic field within the medium in the gap between the surfaces involved. Again, this force can be ignored in practice, as the majority of feedstock is large in size.

2.2 Cohesion Phenomena

Many studies have been conducted to investigate the inter-particle forces affecting particle-particle or particle-wall interactions, but most of these studies have examined only the effects of these forces on fine particles (powders in μm range) in a fluidized bed (Gransden and Sheasby, 1974, Hayashi and Iguchi, 1992, Zhang et al., 2012). However, the intention in the present study is to examine inter-particle forces between spherical large particles (> 5 mm), and in particular, those forces that promote sticking of the particles. In COREX RS, the feedstock contains iron ore pellets, lumps, fluxes and coal. This feedstock is subjected to different types of interactions. The high temperature of the furnace is one of the crucial factors that usually causes a partial melting of some particles (chiefly, smaller ones), which eventually increases the sticking tendency or cohesive forces among solid particles. On the other hand, the concentration of reduced gases also makes an important contribution to process stability, as does the type of oxide ore and its physical and chemical properties.

In COREX, most of the feedstock is in large-size particles, but fine particles may be introduced during transportation of oxides by the friction between particle-particle and particle-wall, or by particle disintegration caused by falling effect or swelling of iron oxides. Most of these events happen at low temperatures (El-Geassy et al., 1996, Higuchi and Heerema, 2005, Wang and Sohn, 2012). These fines fit in between larger particles or simply stick to the furnace wall. An understanding of inter-particle forces between large particles is crucial in order to avoid interruptions to the operation. However, up to now, relatively few studies have been carried out in this area (Higuchi and Heerema, 2005). Fine particles (powders) attract most of the attention; several studies have examined the effect of cohesive forces inside a fluidized bed (see for example (Gransden and Sheasby, 1974, Hayashi and Iguchi, 1992, Zhang et al.,

2012). Cohesion in particulate solids can be classified into two very broad types: wet and dry. In wet cohesion, capillary forces dominate particle interactions. In dry cohesion, for solids of less than 10 μm, van der Waals forces and electrostatic forces are also significant (Chaudhuri et al., 2006).

Many studies have shown that propensity to sticking is promoted or enhanced by multiple factors. Some of these factors relate to operating conditions while others relate to physical and chemical properties of reducing gases and iron ores. These factors may be summarized as follows: (a) In respect of reduction temperature, it was found that iron pellets start to accumulate and stick to each other at higher temperatures (Yi et al., 2013). The transformation from Hematite to Magnetite happens at a very early stage of the reaction, leading with other associated factors (iron precipitations, whisker formation) to increased metallic forces between the particles, and therefore to sticking; (b) Many studies (Wang and Sohn, 2012, Yi et al., 2013, Wang et al., 2012) have shown that reductant gas composition (such as high CO concentration in reductant gas) promotes the sticking tendency, and that this behaviour decreases as H_2 concentration increases. The ratio of these gases (CO and H_2), known as the reductant ratio, was also investigated in the literature; (c) Physical properties of iron pellets, such as porosity and strength, are crucial factors in inhibiting sticking and agglomeration of pellets. Formal investigation by Huang et al. (2012) found that the strength of the pellets decreased dramatically at the beginning of reduction. On the other hand, a certain amount of porosity always enhances the penetration of reductant gases into the pellets, so improving the reduction reaction (Higuchi and Heerema, 2005). However, as porosity increases, pellet strength will decrease, leading to fines production inside the RS. The shape of iron oxides plays an important role in sticking tendency, and spherical shape has the lowest sticking propensity by virtue of the minimal surface contact area; and (d)

Chemical properties of iron oxides are also relevant, and there is evidence that gangue content, particularly in the form of Al_2O_3 and MgO, has a negative impact on sticking, reducing the possibility of forming iron whiskers and decreasing the swelling index (Wang and Sohn, 2011). Again, gangue materials may have positive effects on sticking propensity by decreasing the melting point of iron oxide and so introducing capillary forces between partially melted surfaces. DRI production decreases as a consequence of having to minimize the reduction temperature to overcome low melting point. Clearly, then, sticking can be reduced at the cost of DRI chemistry and productivity of DR plant, with adverse economic and operational consequences for conditions in steel making plants (Basdağ and Arol, 2002). All of the above factors will now be addressed in greater detail.

a) Operational Conditions

The association between high reduction temperature and sticking tendency is well understood (Wang et al., 2012, Yi et al., 2013); as the reduction temperature increases, pellets tend to enlarge, and cracking on pellet surfaces therefore increases, leading to fracture or even spilling of the pellets. Yi et al. (2013) investigated the effect of temperature on sticking index in different reducing gas environments. Figure 2.2 shows that sticking index increased with increasing reduction temperature in all reduction atmospheres.

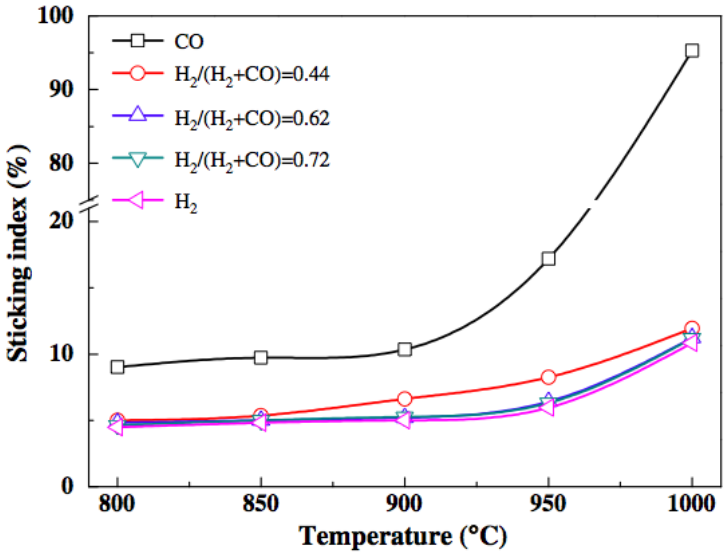

Figure 2.2 : Effect of reduction temperature on sticking index of pellets in different atmospheres (Yi et al., 2013).

As temperature increases to what is known as Tammann temperature (often taken to be half the material's melting point on the absolute temperature scale (Vayenas, 1992)), the amount of precipitated iron increases (Figure 2.3), leading to higher surface energy and causing particles to stick (Zhang et al., 2011). As the temperature changed from 800–900 °C, the sticking indices were identical for each atmosphere. However, sticking index increased noticeably when the temperature increased to 950 °C and then reached the experimental maximum of 1000 °C. It follows that 950 °C can be viewed as a critical temperature on the sticking index.

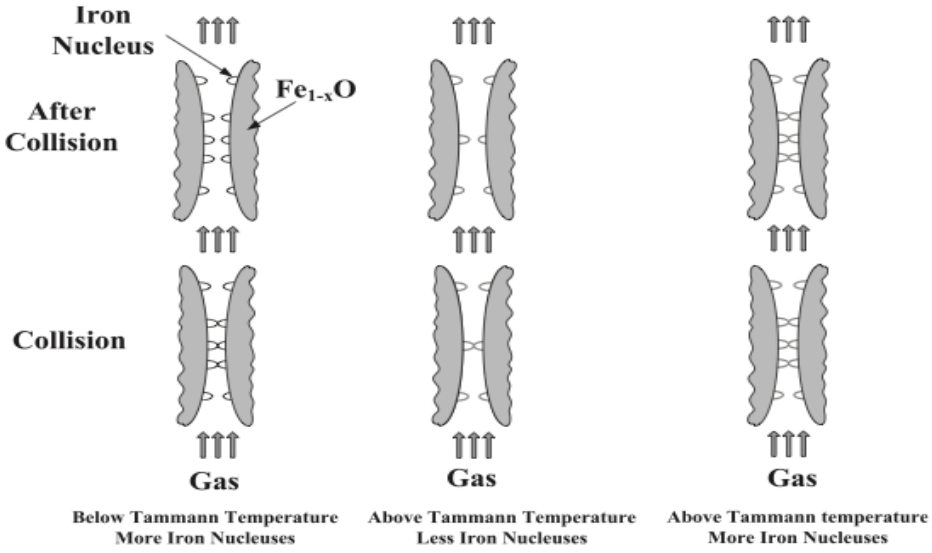

Figure 2.3: Schematic diagram of the mechanism of sticking caused by precipitated iron (Zhang et al., 2011).

With an increasing CO proportion in the reductant gas, the propensity to swelling and sticking will increase (Wang et al., 2012, Yi et al., 2013); the effects of different reductant concentrations on swelling index are shown in Figure 2.4. However, increasing the content of H_2 leads to lower swelling and sticking indices. The effect of CO reducing gas on whisker formation was also investigated by Wang and Sohn (2012), they found that CO reducing gas promotes long whisker formation and therefore increases the swelling index of iron pellets. Another result indicated that sticking time decreased with increasing CO concentration, but the metallization ratio increased. In summary, sticking tendency increased in line with high temperature, CO concentration, reduction potential and gas velocity, respectively (Yi et al., 2013). However, the presence of H_2 in the reducing gas mixture (even at a low concentration of 10%) diminished whisker formation and reduced swelling (Wang and Sohn, 2012).

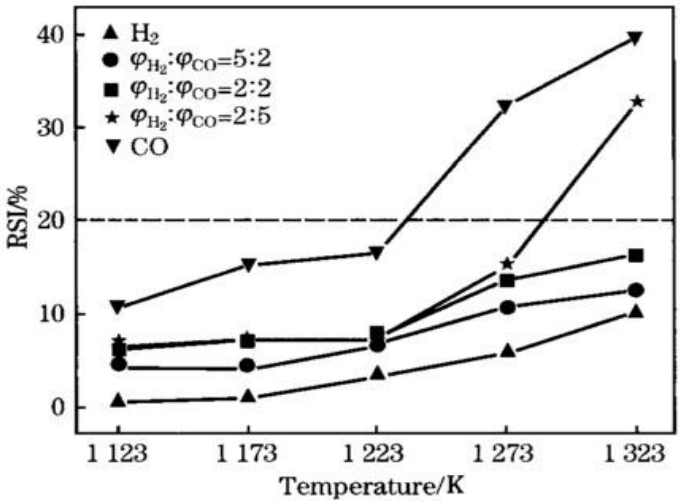

Figure 2.4: Effect of temperature and reductant concentration on swelling index (Wang et al., 2012).

The effects of differential reductant composition and temperature on reduction behaviour are shown in Figure 2.5. As can be seen, a higher H_2 concentration in the reducing gas achieves a faster reduction rate because the molecular diffusion coefficient and reducing power of H_2 are better than those of CO at high temperature (~ > 810 °C).

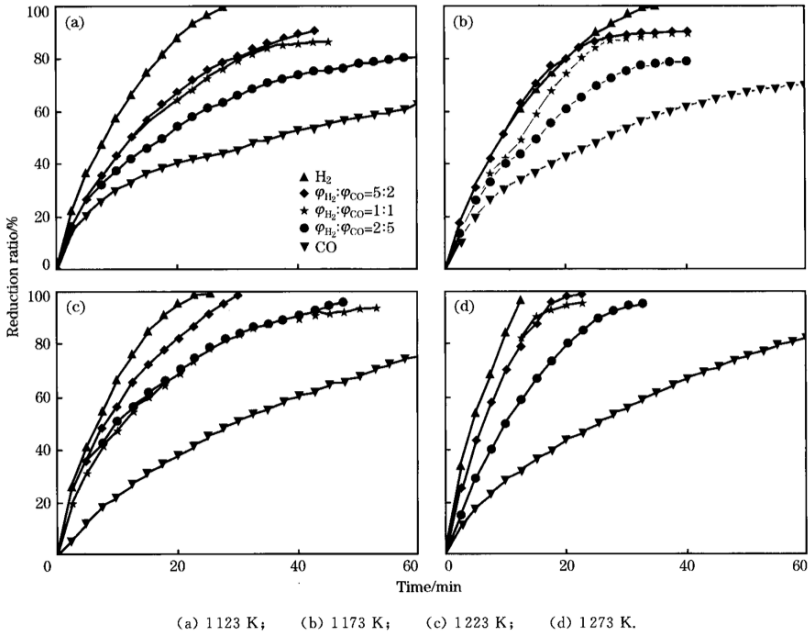

Figure 2.5: Effects of reduction atmosphere and temperature on variation of reduction ratio with time (Wang et al., 2012).

b) Physical Properties

Physical properties of iron oxides such as strength and porosity distributions critically affect the rate of reduction, fines generation and ultimately sticking propensity. Formal investigation by Huang et al. (2012) found that pellet strength decreased dramatically at the beginning of the reduction reaction (from 2800 to 1506 N/Pellet) and then improved slightly when the metallic irons appeared. On the other hand, a certain amount of porosity is always favourable in enhancing the penetration of reductant gases into the pellets and so improves the reduction rate (Higuchi and Heerema, 2005). However, when porosity increases, pellet strength decreases, leading to fines production inside the RS. The shape of iron oxides also plays an important role in determining the sticking tendency; a spherical shape has the lowest sticking propensity because of the minimal surface contact area. Higuchi et al. (2005) proposed two ways of minimizing strength loss during reduction: first, by increasing pore diameter to achieve a lower reduction rate; and second, by increasing pore diameter to form a homogenous reduction, resulting in more uniform stress distribution and less particle expansion during reduction. Wang et al. (2012) found that increasing the CO content of the reducing gas drastically reduced the strength of the pellets at 950 $^{\circ}$C. This phenomenon can be explained as follows. The reduction of oxides by CO is an exothermic reaction, causing temperature variance between the inner and outer surfaces of the pellets. The structure of the pellets also becomes looser after reduction because of the repositioning of carbon during the reaction with CO. Additionally, the binding power among iron grains is diminished when pellets are reduced by CO, resulting in higher porosity and lower strength after reduction.

c) Iron oxides chemistry

While most of the studies were concerned with the external parameters affecting

the reduction and sticking of the pellets, Abdel-Halim et al. (2011) considered the properties of iron oxides as well as external loads applied during the process. Increasing the load allowed for close packing of the particles, which in turn increased the points of contact between metallic irons, enhancing sintering and densification processes. The sticking phenomena were observed only for acidic pellets, where the presence of a silicate phase had a noticeable effect on the enhancement of clustering tendency. Acidic iron ore pellets (0.37 basicity) show a greater tendency to clustering than basic pellets (1.62 basicity). This variation in clustering tendency is most probably related to differences in chemical and mineralogical composition.

On the other hand, gangue contents affect the strength, swelling and sticking behaviours of iron oxide pellets. When the pellets are reduced, the materials undergo volume expansion changes, involving thermal expansion due to heating, phase transformation and growth of iron whiskers during reduction. Where volume change is extreme, the bonding between adjacent planes becomes weak and the pellet cracks. To minimize swelling, the growth of iron whiskers should be restricted. The presence of gangue (SiO_2 and MgO) seems to strengthen pellets by developing slag bonds (Sharma et al., 1990),which is why the swelling index of pure iron oxide pellets is higher than that of non-pure iron (containing gangue). So, as the Fe content of pellets increases, the sticking index increases, as shown in Figure 2.6. However, laboratory tests (Basdağ and Arol, 2002) have shown that certain organic materials like limestone + bentonite, bauxite and serpentine can efficiently be used for this purpose. As a result, pellets with a higher Fe and lower gangue content can be reduced at higher temperatures, leading to productivity improvements.

Unfortunately, gangue materials can also lower the melting point of iron oxides, and any increment in temperature will therefore be limited to prevention of sticking, so

minimizing productivity.

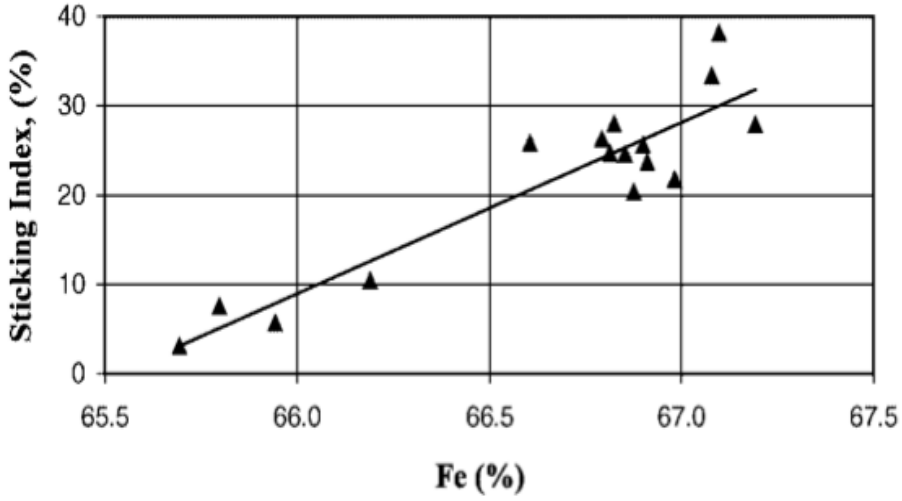

Figure 2.6: Effect of Fe content on sticking of pellets (Basdağ and Arol, 2002).

d) Particle-Wall Interactions

The interaction between particles and the furnace wall is also important. The formation of oxide layers over the wall is a crucial issue in that it may cause production interruption or, in severe cases, may require a major shutdown for removal of these layers. Ortiz et al. (1999) identified the important variables and interactions responsible for the formation of oxide layers over the refractory bricks on the wall of a DRI RS. It is known that various types of cohesive force may account for layer formation. In this case, magnetic attraction was eliminated as the wall refractory was not made of a magnetic material and the iron temperature was higher than the Curie point. Accordingly, Ortiz et al.'s experiments revealed that, at the laboratory scale, shear stress causes layer formation when the powder fines sintered inside the wall pores are accumulated to form layers over the wall. However, adhesion between DRI particles and the wall surface could be avoided by treating the refractory bricks at 1700 °C with silica sand, the purpose being to minimize the porosity of the brick surface. However, unlike those RSs utilized in natural gas-based direct reduction processes, sticking of

iron oxide feedstocks to furnace walls is not a problem in the COREX reduction RS because the reducing gas usually contains coal dust, which serves as a lubricant (Anameric and Kawatra, 2008).

2.3 Computer Simulation

Granular material studies are carried out mainly by conducting conventional experiments to develop the understanding of granular physics; however, particle scale (microscopic) information cannot be gathered by these means. The bulk behaviour of a granular system depends on the collective interactions of individual particles. Particle scale analysis is crucial in establishing the fundamental mechanisms of granular physics. An experimental technique such as PEPT is one of the particle scale research techniques that can measure a single particle trajectory, but it is difficult to obtain all of the micro-dynamic information of particles.

Computer simulations have become increasingly effective as a tool for studying granular materials. The interior state and transient data of a granular flow can readily be examined and measured easily, and simulations can model hypothetical environments that are not easily produced in experiments, such as altered gravity or frictionless particle environments.

2.4 Simulation Methods

In physical simulation area of COREX RS, H. Zhou et al. (2015) studied the effect of a new design called areal gas distribution (AGD) for measuring the solid flow profile in a semi-cylindrical model. The results revealed that the solid flow pattern in the RS model followed a Flat → Wave → W shape profiles as the burden descends. The input gas volume has a minimal effect on solid flow behaviour as well. Additionally, four solid flow zones have been identified as follows; plug flow zone at the top area of

the RS (1), stagnant zone at the lower central part (4), funnel flow zones above the tips of screw dischargers area (2) and quasi-stagnant zone between the funnel flow zone and furnace wall (3), as shown in Figure 2.7.

Figure 2.7: Internal structure of solid flow in COREX RS (1: Plug flow; 2: funnel flow; 3- quasi-stagnant zone; 4- stagnant zone (H. Zhou et al., 2015).

The Monte Carlo method has been widely used as a numerical technique to study particle motions. It was introduced into the field of granular materials in studies of size segregation (Rosato et al., 1986) and varying granular dynamics (Rosato et al., 1987). However, the method has some limitations—for instance, it has no physical time scale, and collision time is assumed to be zero. On the other hand, the normal restitution coefficient must be zero in order to minimize potential energy during each particle move, making it difficult to relate physical material properties to granular dynamics.

Driven by the method of ballistic deposition (Jullien and Meakin, 1987, Jullien and Meakin, 2000), the Method of Steepest Descent can deal with a very large number

of particles. In this kind of simulation, particles reach a local surface minimum after following the path of steepest descent. New particle contacts are treated as completely inelastic collisions. This method was used to study piles with many particles, as well as segregation. Because inertia and elasticity of particles are neglected, and simulation time steps are not connected to physical time, this model is insufficient to describe the full dynamics of granular materials with differing material properties.

Caram and Hong proposed a diffusing void model based on a random walk process of a discrete lattice , which was mostly used to study particle outflow from two-dimensional hoppers (Caram and Hong, 1991, Hong and Caram, 1992). The model makes many assumptions and simplifications, and again does not provide realistic granular dynamics simulation.

A cellular automaton is a discrete model studied in computability theory, mathematics, theoretical biology and microstructure modelling. In these models, space is discretized into cells that have the size of the particles and can be either occupied or empty. The particle dynamics are modelled by a set of particle and collision rules, which apply when certain conditions are satisfied. They have been also used to simulate the behaviour of granular materials during vibration, piling, falling, segregation, displacement of a retaining wall and rapid flow (Kozicki and Tejchman, 2005). The main weakness is that the models are purely kinematic; no flow dynamics is involved, and the underlying physics of the update or collision rules is not clear.

Pioneered by Cundall and Strack in 1979, the discrete element method is perhaps the most common simulation technique. Two types of particle dynamics methods are used in DEM: hard-sphere and soft-sphere. In hard-sphere method, collisions are prompt and binary; in soft-sphere method, collisions are finite and can occur between multiple particles. Soft-sphere method is widely used in granular flow

simulations because most granular flow phenomena have multiple, long-duration particle contacts. The forces acting on each particle in the system are determined and positions of particles are updated.

2.4.1 Discrete Element Method (DEM) and Computational Fluid Dynamics (CFD)

Discrete element method (DEM) (Strack, 1979) is a numerical technique for modelling the multi-body collision behaviour of particulate systems. The principle of DEM is to track, in a time-stepping simulation, the trajectory and rotation of each element in a system to evaluate its position and orientation, and then to calculate the interactions among elements as well as between elements and their surrounding environment. These interactions will subsequently be used to update element positions. In general, elements are individual particles, but they may also represent clusters (Asmar et al., 2002). The motion of each particle in the system in question is described by Newton's equations of motion. The only limiting factor in the DEM approach concerns the limitations of computer capacity. Because the number of particles is so constrained, the method cannot be easily used in real process modelling with the current technology.

In DEM, all forces acting on each particle are modelled and calculated on the basis of the Voigt model, involving a spring-dashpot-slider setup as shown in Figure 2.8. Essentially, the particle *i* is affected by two types of forces: self-gravity and the contact forces due to particle-particle and particle-wall interactions. In addition, the particle *i* is also affected by two torques: the torque due to tangential force and rolling friction torque.

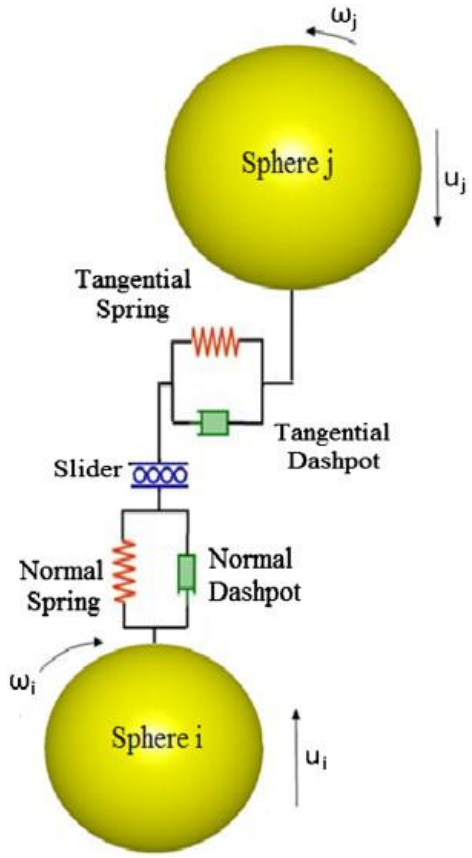

Figure 2.8: Illustration of interaction forces between two particles (Asmar et al., 2002).

Computational Fluid Dynamics (CFD), on the other hand, is an approach that utilizes numerical methods and algorithms to solve and analyze problems that involve fluid flows. The most fundamental consideration in CFD is how to treat a continuous fluid in a discretized way. As pointed out by Yu and Xu (2003), the difficulty in particle-fluid flow modelling relates mainly to solid phase rather than fluid phase. These problems can be solved by coupling CFD and DEM because of its convenience and its capabilities in capturing particle physics behaviours.

This coupling of CFD and DEM is more popular in the study of fluidization. Fluidization is a process of treating solid particles inside a reactor and under appropriate conditions as a fluid-like flow. This is usually achieved when a pressurized gas or liquid is blown upward and evenly through the particulate medium with sufficient force to

cause the particles to rise up and move around inside the reactor so that particles become well mixed with one another and with the liquid or gas. This mixture is then treated as a fluid-like mixture. In the present case, however, the RS is consider as a confined system, as the gravity force of the materials is much higher than the lifting force of the reducing gases**.** An understanding of heat and mass transfer mechanisms is essential to study phenomena involving segregation and sticking tendencies. In CFD-DEM, the motion of discrete particles is obtained by solving Newton's second law of motion as in DEM, and the flow of the continuum fluid is obtained by solving the Navier-Stokes equations, based on the concept of local average as in CFD, coupling CFD and DEM through particle-fluid interaction forces (Xu and Yu, 1997). The main advantage of CFD-DEM is that it can generate detailed particle-scale information, such as the trajectories of and forces acting on individual particles, which is a key to interpreting the mechanisms governing the complicated flow behaviour. With the rapid development of computer technology, the CFD–DEM approach has increasingly been used to study various particle-fluid flow systems (see for example (Ren et al., 2012, Sun et al., 2013, Zhao and Shan, 2013, Zhou et al., 2011).

2.4.2 Applications of CFD-DEM

The CFD-DEM model has been widely used to study the particle-fluid flow observed in almost all types of particulate processes. In process industries, this method is used to gather the following information:

1. Segregation and Mixing efficiency
2. Flow behaviour and jamming
3. Granulation, agglomeration and surface coating
4. Fluidization phenomena and Pneumatic transport
5. Conductive heat transfer and mass transfer

The focus here will be on CFD-DEM applications to blast furnace process.

Mio et al. (2007) built a model of solid particle flow (without gas effect) in the blast furnace. The objective of the model was to analyse solid particle flow in a blast furnace with a bell-type charging system, using large-scale DEM. About 500,000 particles were used in this work. The melting behaviour of iron ore and combustion of coke in an actual blast furnace were modelled by shrinking particles. The results showed a particle pulsating flow in the upper area of the blast furnace, and in this calculation, the descending velocity near the sidewall was much larger than at the centre. The melting position of the ore was mapped, establishing that most of iron ore were melted above the raceway. As shown in Figure 2.9, this area was characterised as the cohesive zone.

Figure 2.9: Mapping of mass of melted ore (Mio et al., 2007).

Zhou et al. (2011) analysed gas-solid flow in a blast furnace by combining discrete particle simulation (DPS) or DEM with computational fluid dynamics (CFD). The conditions considered included different gas and solid flow rates, asymmetric conditions such as non-uniform gas and solid flow rates in blast furnace raceways and existence of

scabs on the sidewalls. The model was able to capture blast furnace solid flow patterns (Figure 2.10, as well as microscopic-level information about particles such as porosity, velocity and force structure (Figure 2.11). The results revealed that stagnant zone size increases with increasing gas flow rate or with decreasing solid flow rate. The results also showed that solid pressure and porosity vary spatially. Generally, solid pressure increases from top to bottom on the central axis. Porosity increases from the top to the stagnant zone on the central axis, and from the top sidewall to the central region, but decreases from the raceway to its surroundings. Three regions were identified (Figure 2.12): region I (plug flow zone), where solid pressure increases with the increase of porosity; region II (quasi-stagnant zone and stagnant zone), where solid pressure scatters and varies within a large range; and region III (vicinity of raceway), where solid pressure decreases with increasing porosity.

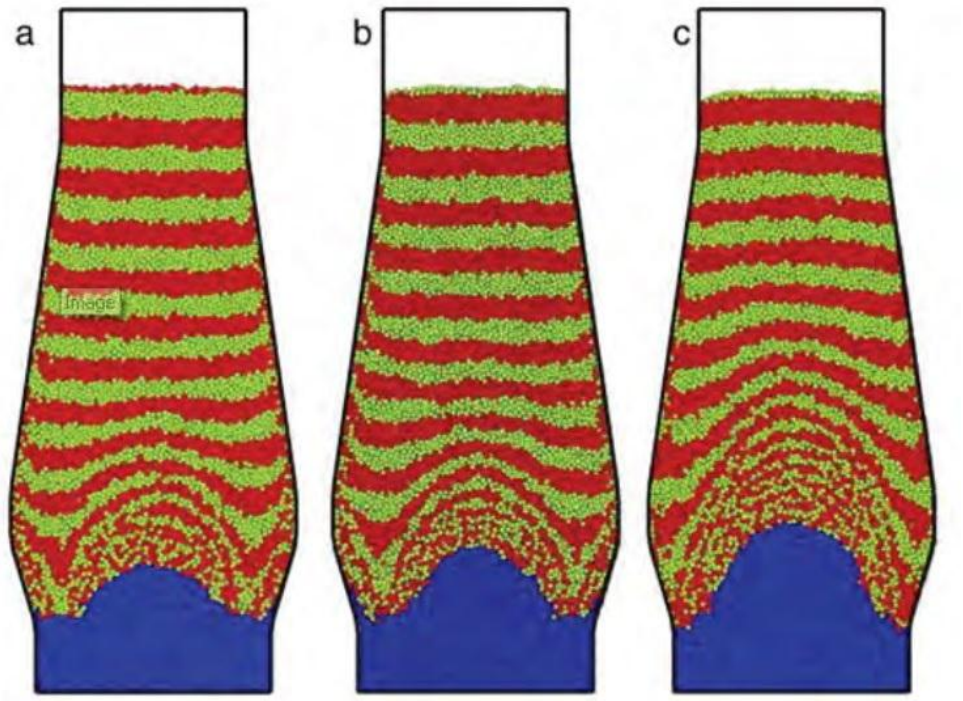

Figure 2.10: Solid flow patterns for different gas flow rates: (a) 0 m3/s; (b) 1.93×10^{-2} m^3/s; and (c) 5.79×10^{-2} m^3/s when the solid flow rate is 0.3 kg/s (Zhou et al., 2011).

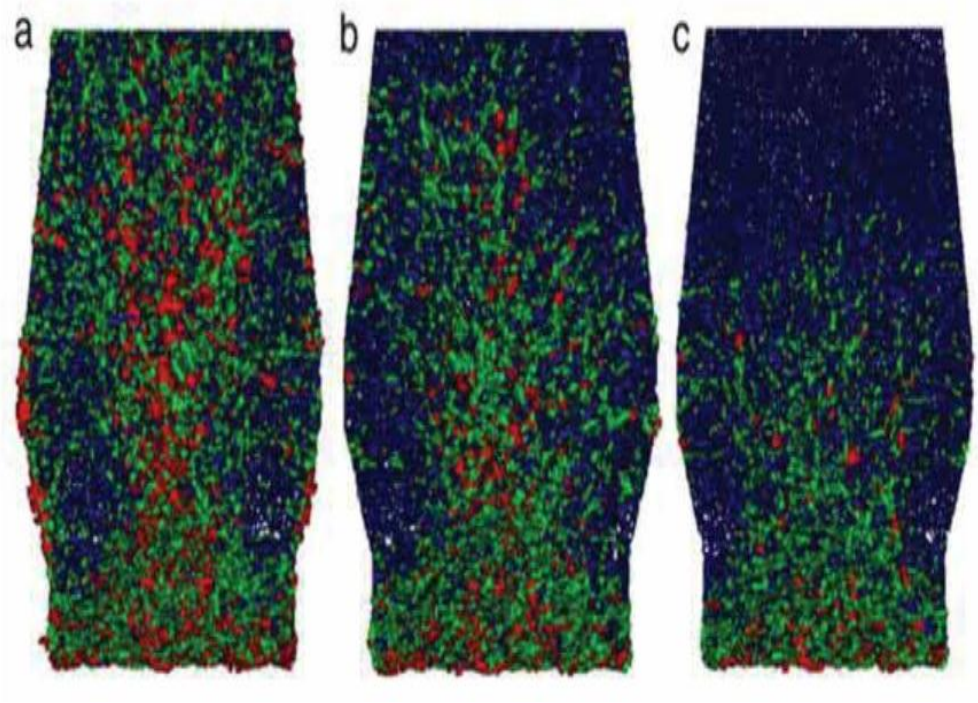

Figure 2.11: Normal force network for different gas flow rates: (a) 1.93×10^{-2} m^3/s; (b) 5.79×10^{-2} m^3/s; and (c) 6.94×10^{-2} m^3/s when the solid flow rate is 0.3 kg/s (Zhou et al., 2011).

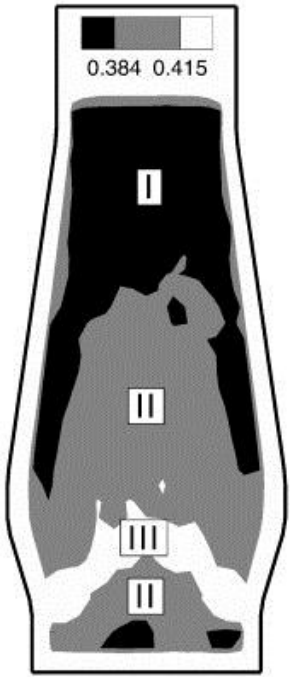

Figure 2.12: Spatial distribution of porosity corresponding to the three regions (Zhou et al., 2011).

Xu et al. (2000) analysed the gas solid flow in a raceway that was formed by lateral gas blasting. The model simulated the motion of 10,000 spherical particles of 4 mm diameter. It was shown that, depending on gas velocity, the bed could be transformed

from fixed to fluidized or vice versa; particle velocity and motion could be described by a CFD-DEM model, as shown in Figure 2.13. Results also showed that large particle-particle contact forces occurred along the boundary between the moving and stagnant zones while large fluid drag forces occurred in the roof of the raceway.

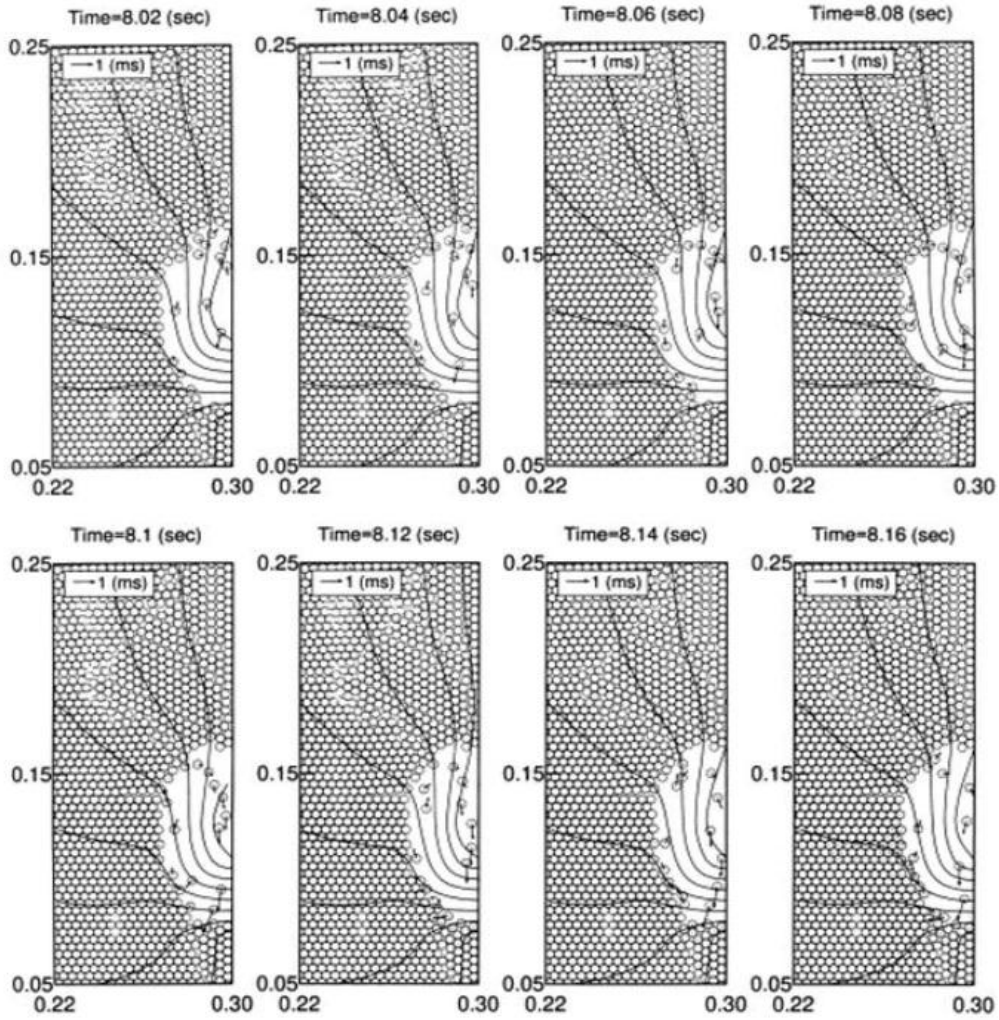

Figure 2.13: Gas streamlines and particle velocity showing the circulating flow of particles in the raceway when gas velocity is 25 m/s (Xu et al., 2000).

Chapter 3 MODEL DESCRIPTION

In the present study, the CFD-DEM method is used to investigate and analyse gas-solid flow, heat transfer and the effects of cohesive force on the flow in the COREX RS. The advantages of this method were outlined previously in Chapter 2. Here, the specific governing equations of CFD and DEM are described.

3.1 Governing Equations for DEM

In this study, gas-solid flow in the RS is considered to be composed of a discrete solid phase, which is analysed by DEM, and a continuum gas phase, which is described by CFD. In DEM, each individual particle has two types of motion: rotational and translational. While moving, and at every time step, the particle may interact with its neighbouring particles and/or adjacent wall, through which energy and momentum exchange takes place. At any given time *t*, the equations governing the motions of particle *i* of mass m_i and radius R_i can be described as:

$$m_i \, dv_i / dt = \sum_j (\mathbf{f}_{e,ij} + \mathbf{f}_{d,ij} + \mathbf{f}_{c,ij}) + \mathbf{f}_{pf,i} + m_i \mathbf{g}, \tag{3.1}$$

and

$$I_i \, d\boldsymbol{\omega}_i / dt = \sum_j (\mathbf{T}_{t,ij} + \mathbf{T}_{r,ij}), \tag{3.2}$$

where $\mathbf{v}_i$ and $\boldsymbol{\omega}_i$ are the translational and rotational velocities, and I_i $(= 2/5 m_i R_i^2)$ is the moment of inertia of the particle. The forces involved are: the particle-fluid interaction force $\mathbf{f}_{pf,i}$; the gravitational force $m_i\mathbf{g}$; and the forces between particles (and between particles and walls), which include the elastic force $\mathbf{f}_{e,ij}$, the viscous damping force $\mathbf{f}_{d,ij}$ and the cohesive force $\mathbf{f}_{c,ij}$. The torque acting on particle *i* due to particle *j* includes two components: $\mathbf{T}_{t,ij}$, which is generated by the tangential force and causes particle *i* to rotate; and $\mathbf{T}_{r,ij}$, commonly known as the rolling friction torque, which is generated by

the asymmetric normal contact forces and slows down the relative rotation between contacting particles. If particle *i* undergoes multiple interactions, the individual interaction forces and torques are summed for all particles interacting with particle *i*. Figure 3.1 shows the forces and torques schematically.

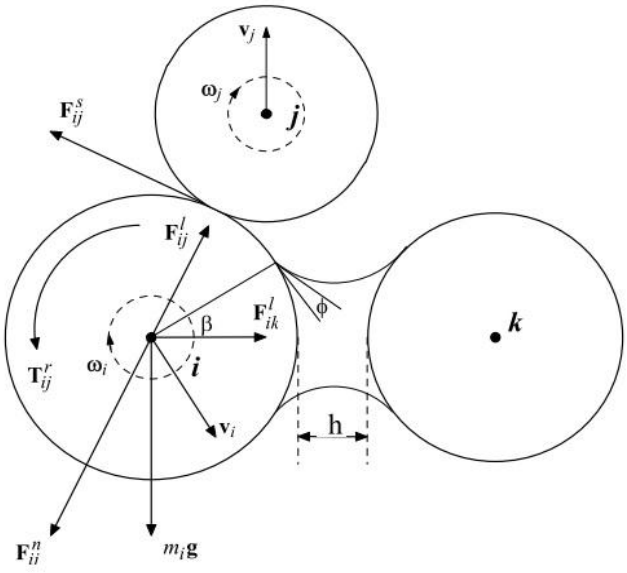

Figure 3.1: Schematic illustration of the forces acting on particle *i* from contacting particle *j* and non-contacting particle *k* (capillary force here) (Zhu et al., 2007).

The equations used in this model are well described in the literature (Zhu et al., 2007) and are summarized here in Table 3.1 (Hou et al., 2012c). Once the forces and torques are obtained, the equations (3.1) and (3.2) can be solved, and the motion information for particles, including trajectories, velocities and transient forces, can be determined.

Table 3.1: List of equations to calculate forces and torques on particle *i* (Hou et al., 2012c).

Force or Torque	**Equation**
Normal elastic force, $\mathbf{f}_{en,ij}$	$-\frac{4}{3}E^*\sqrt{R^*}\delta_n^{3/2}\mathbf{n}$
Normal damping force, $\mathbf{f}_{dn,ij}$	$-c_n\left(6m_{ij}E^*\sqrt{R^*\delta_n}\right)^{1/2}\mathbf{v}_{n,ij}$
Tangential elastic force, $\mathbf{f}_{et,ij}$	$-\mu_s\left\|\mathbf{f}_{en,ij}\right\|(1-(1-\delta_t/\delta_{t,\max})^{3/2})\hat{\boldsymbol{\delta}}_t$
Tangential damping force, $\mathbf{f}_{dt,ij}$	$-c_t\left(6\mu_s m_{ij}\left\|\mathbf{f}_{en,ij}\right\|\sqrt{1-\delta_t/\delta_{t,\max}}/\delta_{t,\max}\right)^{1/2}\mathbf{v}_{t,ij}$
Coulomb friction force, $\mathbf{f}_{t,ij}$	$-\mu_s\left\|\mathbf{f}_{en,ij}\right\|\hat{\boldsymbol{\delta}}_t$
Torque by tangential forces, $\mathbf{T}_{t,ij}$	$\mathbf{R}_{ij}\times\left(\mathbf{f}_{et,ij}+\mathbf{f}_{dt,ij}\right)$
Rolling friction torque, $\mathbf{T}_{r,ij}$	$\mu_{r,ij}\left\|\mathbf{f}_{en,ij}\right\|\hat{\boldsymbol{\omega}}_{ij}^n$
Particle-fluid drag force, $\mathbf{f}_{d,i}$	$0.125C_{d0,i}\rho_f\pi d_{pi}^2\varepsilon_i^2\left\|\mathbf{u}_i-\mathbf{v}_i\right\|(\mathbf{u}_i-\mathbf{v}_i)\varepsilon_i^{-\chi}$
Pressure gradient force, $\mathbf{f}_{pg,i}$	$-V_i\nabla p_i$

where $1/m_{ij}=1/m_i+1/m_j$, $1/R^*=1/\mathrm{R}_i+1/\mathrm{R}_j$, $E^*=E/[2(1-\nu^2)]$, $\hat{\boldsymbol{\omega}}_{ij}^n=\boldsymbol{\omega}_{ij}^n/\left|\boldsymbol{\omega}_{ij}^n\right|$,

$\delta_t=\left|\boldsymbol{\delta}_t\right|$, $\hat{\boldsymbol{\delta}}_t=\boldsymbol{\delta}_t/\left|\boldsymbol{\delta}_t\right|$, $\mathbf{R}_{ij}=R_i(\mathbf{r}_j-\mathbf{r}_i)/(R_i+R_j)$, $\delta_{t,\max}=\mu_s\delta_n(2-\nu)/(2(1-\nu))$,

$\mathbf{v}_{ij}=\mathbf{v}_j-\mathbf{v}_i+\boldsymbol{\omega}_j\times\mathbf{R}_j-\boldsymbol{\omega}_i\times\mathbf{R}_i$, $\mathbf{v}_{n,ij}=(\mathbf{v}_{ij}\cdot\mathbf{n})\cdot\mathbf{n}$, $\mathbf{v}_{t,ij}=(\mathbf{v}_{ij}\times\mathbf{n})\times\mathbf{n}$, $\varepsilon_i=1-\sum_{i=1}^{k_v}V_i/\Delta V$,

$\chi=3.7-0.65\exp[-(1.5-\log_{10}\mathrm{Re}_i)^2/2]$, $C_{d0,i}=(0.63+4.8/\mathrm{Re}_i^{0.5})^2$,

$\mathrm{Re}_i=\rho_f d_{pi}\varepsilon_i\left|\mathbf{u}_i-\mathbf{v}_i\right|/\mu_f$.

Note that tangential forces ($\mathbf{f}_{et,ij}$ + $\mathbf{f}_{dt,ij}$) should be replaced by $\mathbf{f}_{t,\ ij}$ when $\delta_t\geq\delta_{t,\max}$

3.2 Governing Equations for CFD

The fluid phase in this study is described by the CFD method. In CFD, the fluid domain is discretized into cells, as seen for 1D and 2D cases in Figure 3.2. In each cell, all variables such as fluid velocity, pressure and density are locally averaged quantities. There are, then, three sets of governing equations as first developed by Anderson and Jackson (1967) and then further modified by (Xu and Yu, 1997, Zhou et al., 2010, Feng and Yu, 2004).

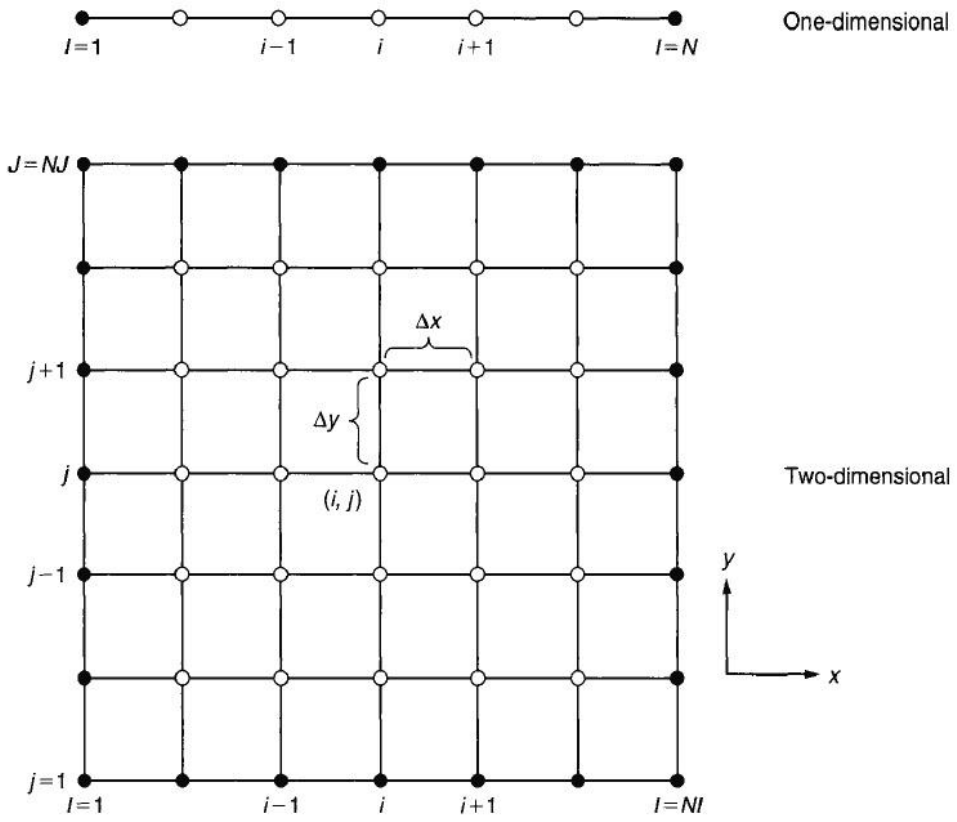

Figure 3.2: A representation of one-dimensional and two-dimensional uniformly distributed Cartesian cells.

In Set I, the fluid governing equation is derived directly, based on the point equation of motion of the fluid and the solid phase governing equation, on the basis of the equation of motion for the centre of mass of a single particle. In Set II, in order to solve the undetermined terms, Anderson and Jackson (1967) formulated some constitutive equations for the solid stress tensor and decomposed the particle-fluid interaction force into two components, at 'macroscopic' and particle scales. To eliminate the fluid stress

tensor in the solid phase governing equation in Set II, Set III is derived on the assumption that fluid flow through the particle phase should be steady and uniform. According to Zhou et al. (2010), Set II and in particular Set I can be used generally while Set III can be used only conditionally. In the present case, Set I is used. Accordingly, the governing equations comply with the conservation of mass and momentum over computational cells, based on the local-average method for a computational cell, which can be written as

$$\partial(\rho_f \varepsilon_f)/\partial t + \nabla \cdot (\rho_f \varepsilon_f \mathbf{u}) = 0, \tag{3.3}$$

and

$$\partial(\rho_f \varepsilon_f \mathbf{u})/\partial t + \nabla \cdot (\rho_f \varepsilon_f \mathbf{u}\mathbf{u}) = -\nabla p - \mathbf{F}_{fp} + \nabla \cdot \boldsymbol{\tau} + \rho_f \varepsilon_f \mathbf{g}, \tag{3.4}$$

where $\mathbf{u}$, ρ_f, and p are the fluid velocity, density and pressure, respectively; $\mathbf{F}_{fp}$ is the volumetric fluid-particle interaction force; and $\boldsymbol{\tau}$ and ε are the fluid viscous stress tensor and porosity of a computational cell, given as:

$$\boldsymbol{\tau} = \boldsymbol{\mu_e}[(\boldsymbol{\nabla_u}) + (\boldsymbol{\nabla_u})^{-1}], \tag{3.5}$$

$$\boldsymbol{\varepsilon} = \mathbf{1} - \left(\sum_{j=1}^{k_c} \boldsymbol{V_i}\right)/\Delta \boldsymbol{V}, \tag{3.6}$$

where μ_e is the fluid molecular viscosity and V_i is the volume of particle *i*.

3.3 Calculation of Particle-Fluid Interaction Force

The particle-fluid interaction force $\mathbf{F}_{Pf,i}$ is the sum of all kinds of particle-fluid interaction forces acting on single particles by fluid, including fluid drag force, pressure gradient force, viscous force, virtual mass force, basset force and lift force (Zhu et al., 2007). The drag force $\mathbf{F}_{d,i}$ and the pressure gradient force $\mathbf{F}_p$ are considered here, the drag forces on a single particle *i* can be written as:

$$\boldsymbol{F_{d,i}} = \boldsymbol{F_{f0,i}\varepsilon_i^{-(x+1)}} \tag{3.7}$$

where ε_i is the porosity around particle i; $F_{f0,i}$ is the fluid drag force on particle i in the absence of other particles; and x is the coefficient, given by:

$$\boldsymbol{F_{f0,i} = 0.5 C_{d0,i} \rho_f \pi R_i^2 \varepsilon_i^2 |\mathbf{u}_i - \mathbf{v}_i| (\mathbf{u}_i - \mathbf{v}_i)} \tag{3.8}$$

$$\boldsymbol{x = 3.7 - 0.65 \exp[-(1.5 - \log_{10} Re_i)^2 / 2]} \tag{3.9}$$

The fluid drag coefficient $C_{d0,i}$ and the particle Reynolds number Re_i are given as

$$\boldsymbol{C_{d0,i} = (0.63 + 4.8 / Re_i^{0.5})^2} \tag{3.10}$$

$$\boldsymbol{Re_i = \rho_f d_i \varepsilon_i |\mathbf{u}_i - \mathbf{v}_i| / \mu_f} \tag{3.11}$$

and the pressure gradient force $\mathbf{F}_p$ can be written as

$$\boldsymbol{F_p = -V_p \cdot \nabla \mathbf{p}} \tag{3.12}$$

After particle-fluid drag forces and the pressure gradient force on a single particle have been determined, the volumetric particle-fluid drag force in a computational cell can be determined by:

$$\boldsymbol{F_{pf,i} = \sum_{i=1}^{k_c} (F_{d,i} + F_p) / \Delta V} \tag{3.13}$$

3.4 Coupling Scheme of CFD and DEM Methods

In the CFD-DEM coupling approach, the motion of individual particles is acquired by solving Newton's equations while fluid flow is determined by CFD at the computational cell scale (Hoomans et al., 1996, Tsuji et al., 1993). As pointed out by Xu and Yu (1997), the coupling of CFD and DEM methods can be achieved mathematically as follows. At each time step, DEM will determine the positions and velocities of individual particles for the evaluation of porosity and volumetric fluid drag force in a computational cell. CFD will use these data to determine the fluid flow field and will then calculate the fluid drag forces acting on individual particles. Incorporation

of the resulting forces into DEM will produce information about the motion of individual particles for the next time step.

3.5 Heat Transfer Model

Heat transfer between particle *i* and its surroundings involves three heat transfer mechanisms: particle-fluid convection, particle-particle or particle-wall conduction and particle radiation. According to the energy balance, the governing equation for particle *i* can be generally written as (Zhou et al., 2009, Hou et al., 2012b, Hou et al., 2012a)

$$\boldsymbol{m_i c_{p,i} \frac{dT_i}{dt} = \sum_{j=1}^{k_i} \dot{Q}_{i,j} + \dot{Q}_{i,f} + \dot{Q}_{i,rad} + \dot{Q}_{i,wall}} \quad (3.14)$$

where $\dot{Q}_{i,j}$ is the heat exchange rate between particles *i* and *j* due to conduction; $\dot{Q}_{i,f}$ is the heat exchange rate between particle *i* and its surrounding fluid; $\dot{Q}_{i,rad}$ is the heat exchange rate between particle *i* and its surrounding environment by radiation; $\dot{Q}_{i,wall}$ is the heat exchange rate between particle *i* and the wall; k_i is the number of particles exchanging heat with particle *i*; and $c_{p,i}$ is the particle specific heat at constant pressure. The detail of each mechanism as noted by Zhou et al. (2009) is addressed here as follows.

a) Convective Heat Transfer

The convective heat transfer rate between particle *i* and fluid is commonly calculated according to eq. 3-15:

$$\boldsymbol{\dot{Q}_{i,f} = h_{i,conv} A_i (T_{f,i} - T_i)} \quad (3\text{-}15)$$

where A_i is the particle surface area; $T_{f,i}$ is the fluid temperature inside a computational cell where particle *i* is located; and $h_{i,conv}$ is the convective heat transfer coefficient (HTC). $h_{i,conv}$ is related to the Nusselt number, a function of the particle Reynolds number and the gas Prandtl number, which is given by

$$\boldsymbol{Nu_i = \frac{h_{i,conv} d_{pi}}{k_f} = 2.0 + aRe_i^b Pr^{1/3}} \quad (3\text{-}16)$$

where k_f and d_{pi} are the fluid thermal conductivity and partial diameter, respectively, and Re_i is the local relative Reynolds number for particle *i*. The variation of Prandtl number is minor with temperature and here the value is set to 0.712 at 300K. The constant, 2.0, represents the contribution from particle-fluid natural convection; a = 1.2, and b = 0.5 are assumptions based on the recent literature data; 2.0 represents the contribution from particle-fluid natural convection.

The equation used to determine the fluid-wall heat transfer coefficient $h_{f,wall}$ is

$$\boldsymbol{N_{uD} = \frac{h_{f,wall} D}{k_f} = 0.023 Re^{0.8} Pr^n} \quad (3\text{-}17)$$

where D is the hydraulic diameter, and the exponent n is 0.4 for heating and 0.3 for cooling. Then, the heat flux $\dot{Q}_{f,wall}$ between particle and wall is determined by

$$\boldsymbol{\dot{Q}_{f,wall} = h_{f,wall} \cdot A_{f,wall} \cdot (T_{wall} - T_f)} \quad (3\text{-}18)$$

where $A_{f,wall}$ is the contact area between fluid and wall.

b) Conductive Heat Transfer

Most conduction between particles involves particle-fluid-particle conduction heat transfer and particle-particle conduction heat transfer.

- *Particle-fluid-particle conduction heat transfer*

  The particle-fluid-particle heat transfer model used here is the one proposed by Cheng et al. (1999) with some modifications as proposed by (Zhou et al., 2009). Figure 3.3 shows the contact conditions between two adjacent particles *i* and *j*. T_i and T_j are the temperatures of particles *i* and *j* respectively. The heat flux between particles can be described as:

$$\dot{Q}_{ij} = (T_j - T_i) \int_{r_{sij}}^{r_{sf}} \frac{2\pi \cdot r dr}{(\sqrt{R^2 - r^2}) - \frac{r(R+H)}{r_{ij}} \cdot \left(\frac{1}{k_{pi}} + \frac{1}{k_{pj}}\right) + 2[(R+H) - \sqrt{R^2 - r^2}]/k_f} \tag{3.19a}$$

where

$$H = \frac{d_{ij} - 2R}{2} \tag{3.20b}$$

$$r_{sf} = \frac{R \cdot r_{ij}}{\sqrt{r_{ij}^2 + (R+H)^2}} \tag{3.19c}$$

$$r_{ij} = 0.560 R_i (1 - \varepsilon_i)^{-2/3} \tag{3.19d}$$

and where k_{pi} and k_{pj} are the thermal conductivities of particles *i* and *j*, respectively. As shown in Figure 3.3, parameter r_{sij} = 0 when $H \geqslant 0$ and $r_{sij} = r_c$ when $H < 0$, where r_c is the radius of the contact area of two contacting particles; r_{ij} is the radius of the lens of fluid between two contacting or near-contacting spheres; ε_i is the local porosity of particle *i*; and d_{ij} is obtained from DEM simulation. When the distance of 2*H* is greater than the particle radius *R*, heat flux between the two particles can be ignored.

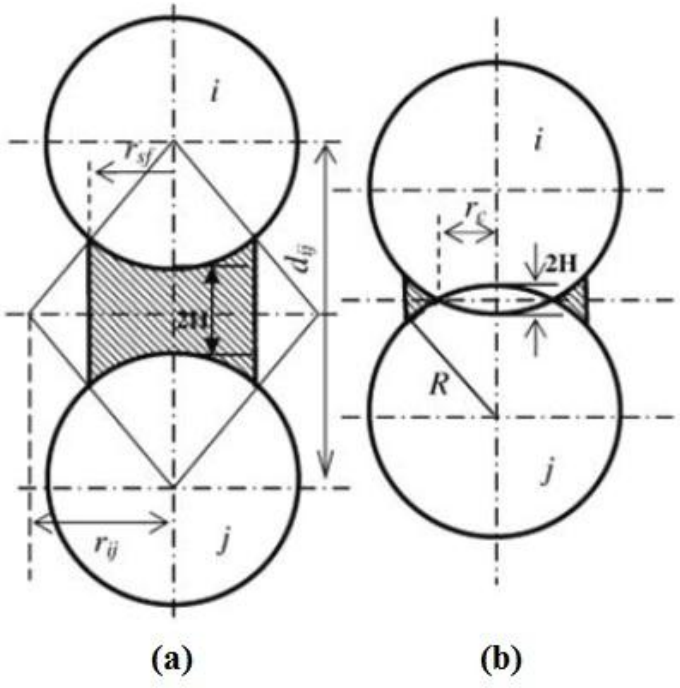

Figure 3.3: Relative positions of two spheres: (a) non-contact case; (b) contact with overlap case (Zhou et al., 2009).

- *Particle-particle conduction heat transfer*

Conduction heat transfer occurs between two solid materials: particle-particle or particle-wall. Generally, conduction due to elastic deformation involves two mechanisms: conduction due to particle-particle static contact (i.e. packed bed condition), and conduction due to particle-particle collision, which is common in a moving or fluidized bed reactor (Zhou et al., 2009). In conduction due to particle-particle static contact, equation 3-20 is adopted as first proposed by Batchelor and Brien (1977) and subsequently modified by Cheng et al. (1999). This equation is used to calculate heat flux through the contact area between particles *i* and *j* as follows:

$$\dot{\boldsymbol{Q}}_{\boldsymbol{i,j}} = \frac{\boldsymbol{4r_c(T_j - T_i)}}{\left(\frac{\boldsymbol{1}}{\boldsymbol{k_{pi}}} + \frac{\boldsymbol{1}}{\boldsymbol{k_{pj}}}\right)} \tag{3.20}$$

The equations used to determine particle-particle collision were first proposed by Sun and Chen (1988) and subsequently modified by Zhou et el. (2008a) for ease of implementation in the CFD-DEM model:

$$\dot{\boldsymbol{Q}}_{\boldsymbol{i,j}} = \boldsymbol{c'} \frac{\boldsymbol{(T_j - T_i)\pi r_c^2 t_c^{-1/2}}}{\boldsymbol{(\rho_{pi} c_{pi} k_{pi})^{-1/2} + (\rho_{pj} c_{pj} k_{pj})^{-1/2}}} \tag{3.21a}$$

$$c' = 0.435 \cdot \left(\sqrt{c_2^2 - 4c_1(c_3 - F_0)} - c_2\right)/c_1 \tag{3.21b}$$

$$c_1 = -2.300 \cdot \left(\frac{\rho_{pi} c_{pi}}{\rho_{pj} c_{pj}}\right)^2 + 8.909 \cdot \left(\frac{\rho_{pi} c_{pi}}{\rho_{pj} c_{pj}}\right) - 4.235 \tag{3.21c}$$

$$c_2 = 8.169 \cdot \left(\frac{\rho_{pi} c_{pi}}{\rho_{pj} c_{pj}}\right)^2 - 33.770 \cdot \left(\frac{\rho_{pi} c_{pi}}{\rho_{pj} c_{pj}}\right) + 24.885 \tag{3.21d}$$

$$c_3 = -5.758 \cdot \left(\frac{\rho_{pi} c_{pi}}{\rho_{pj} c_{pj}}\right)^2 + 24.464 \cdot \left(\frac{\rho_{pi} c_{pi}}{\rho_{pj} c_{pj}}\right) - 20.511 \tag{3.21e}$$

$$t_c = 2.94 \left(\frac{5m_{ij}}{4E_{ij}}\right)^{\frac{2}{5}} (R_{ij} \cdot v_{nij})^{-1/5} \tag{3.21f}$$

where r_c and t_c are particle-particle contact radius and collision duration, respectively; *Fo* is the Fourier number and can be defined as $a \cdot t_c / r_c^2$, where a is particle thermal diffusivity; v_{nij} is the normal relative velocity between particles *i*

and *j*. For heat transfer through particle-wall contact, a wall can be treated as a particle whose mass and properties are the same as the other particles used here. t_c can be obtained by equation 3.21f; t_d is the particle-particle contact duration time, which can be obtained from simulation. The specific calculation scheme used here is that for two colliding particles; if $t_c \geq t_d$, only collisional heat transfer applies. If $t_c < t_d$, two particles will remain stuck together after collision. In this case, collision heat transfer applies first during the time t_c, and then static heat transfer applies during the time (t_d - t_c).

- *Radiative heat transfer*

Inside the RS, a particle is surrounded by particles and fluid. In radiative heat transfer, however, the heat transfer between a particle and its environment is described as:

$$\dot{\boldsymbol{Q}}_{\boldsymbol{i,rad}} = \boldsymbol{\sigma \varepsilon_{pi} A_i (T^4_{local,i} - T^4_i)} \tag{3.22}$$

where σ is the Stefan-Boltzmann constant equal to 5.67 x 10^{-8} W/(m^2.K^4), and ε_{pi} is the sphere emissivity (set to 0.8 in the present case). Gas radiation is ignored in this study because gas emissivity is low.

The parameter $T_{local,i}$ is the averaged temperature of particles and fluid by volume fraction in an enclosed spherical domain Ω given by:

$$\boldsymbol{T_{local,i} = \varepsilon_f T_{f,\Omega} + (1 - \varepsilon_f) \frac{1}{k_\Omega} \sum_{j=1}^{k_\Omega} T_j (j \neq 1)} \tag{3.23}$$

where $T_{f,\Omega}$ is the fluid temperature and k_Ω is the number of particles located in the domain Ω. For present purposes, the domain radius is assumed to be $2d_p$.

Chapter 4 GAS-SOLID FLOW IN REDUCTION SHAFT

Some parts of this Chapter were published on ISIJ International Journal with title "*Modelling the Gas-solid Flow in the Reduction Shaft of COREX"; Qin-Fu HOU, Mohammed SAMMAN, Jian LI and Ai-Bing YU. ISIJ International, Vol. 54 (2014), No. 8, pp. 1772–1780*

Three phases (solid, gas and powder) are generated in the RS; powders or fines are a minor occurrence in the system and can be safely ignored here. The RS itself is a tube-like reactor, approximately 18 m in height and 7.8 m in diameter at its base, as shown in Figure 4.1.

Figure 4.1: Reduction shaft (RS) of COREX process.

In this process, the iron oxides and coal are charged from the top while reducing gases are injected from the lower part of the RS. Solids and gases react in counter-current interactions to produce DRI, which is then discharged into the melter-gasifier by the screw feeders at the bottom of the RS. Understanding the gas-solid flow of the RS process is of great importance for improving the stability of the system and for enhancing overall operating efficiency. In this chapter, an attempt will be made to understand the gas-solid flow inside the RS at different gas flow velocities.

4.1 Simulation Conditions

Here, a 2-D CFD-DEM slot model (Figure 4.2) is used to examine the gas-solid flow at different gas velocity conditions. The numerical method for CFD-DEM simulation has already been detailed in Chapter 3, and the coupling scheme was set out in section 3.4.

A scaled-down model was used here: one quarter of the size of a practical RS, (as illustrated in Figure 4.2) with a larger particle size of 60 mm diameter, as is common practice in DEM or CFD-DEM simulations in order to overcome computing limitations. Two particle types are used: iron and coke. It is expected that the effect of density is insignificant in the dense flow regime, so the particles' properties are assumed in both cases to be the same as those of iron, and are listed in Table **4.1**. Two gas inlets and two discharging zones are represented schematically in Figure 4.2. In practice, inclined inlets are adopted. One of the important advantages of such a design is to reduce the chocking risk by fine powders. However, because the discharging screw feeder outlets are normally well sealed the development of downward gas flow is limited. Furthermore, all particles used in the simulation are of large size and the focus is not on choking phenomena. For the present study of heat transfer in the transient gas-solid flow, it is assumed for simplicity that the effect of inclined inlets is insignificant. Further study will be conducted to examine whether the effect of such a design is significant on heat transfer. Gas is charged at the inlets and particles are removed from the discharging zones and recycled to the top. The standard gas velocity (4 m/s in this case) is based on the real gas flowrate in plant operation and the ratio between the volumes of the real system and the scaled-down model. To eliminate the effect of walls, periodic boundary conditions are applied to the solid phase along the front and rear boundaries as illustrated in Figure 4.3.

Table 4.1: Particle properties used in CFD-DEM model.

Particle diameter d_p, mm	60
Bed thickness, mm	$4d_p$
Density ρ_p, kg/m^3	2500
Young's modules, Pa	1×10^7
Poisson's ratio, -	0.3
Friction coefficient, -	0.3
Restitution coefficient, -	0.8
Time step, s	7.50×10^{-5}
Total number, -	25000

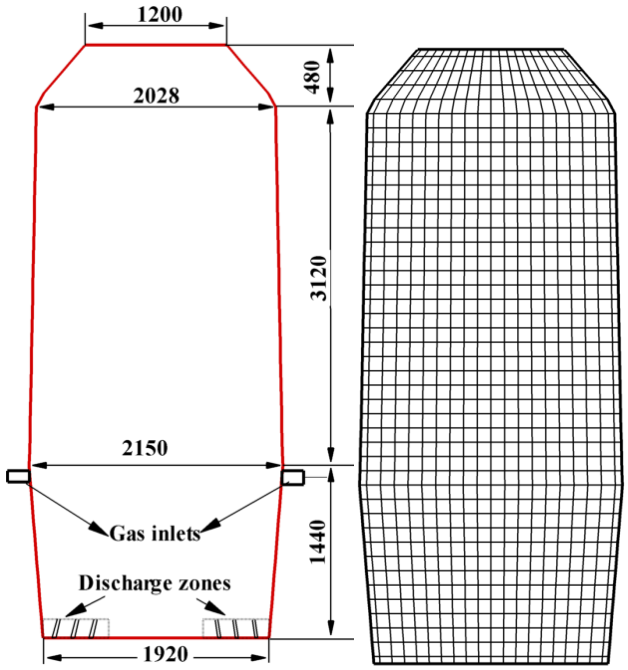

Figure 4.2: 2D slot model of RS (dimensions in mm) and CFD mesh (20 × 44).

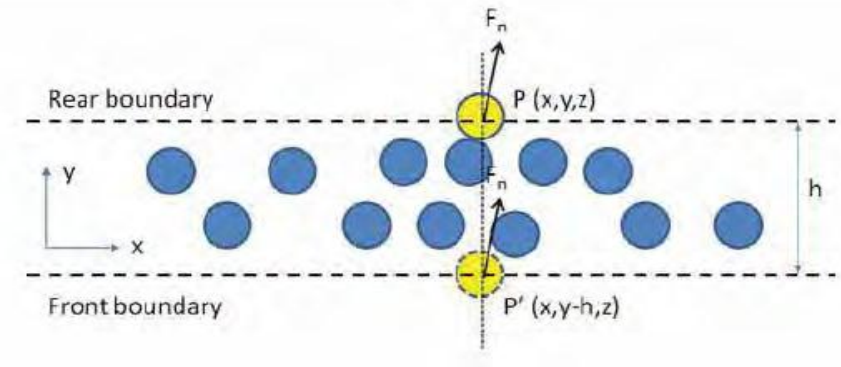

Figure 4.3: Schematic illustration of periodic boundary condition.

4.2 Effect of Gas Flow

To investigate coupled gas-solid flow in the 2-D slot model, the effect of gas flow was examined at different inlet gas velocities with the particle discharge rate fixed at 36.14 kg/s in order to obtain a stable flow configuration for a short period.

The initial packed bed is shown in Figure 4.4, followed by snapshots of flow patterns at an inlet gas velocity of 2 m/s (Figure 4.5).

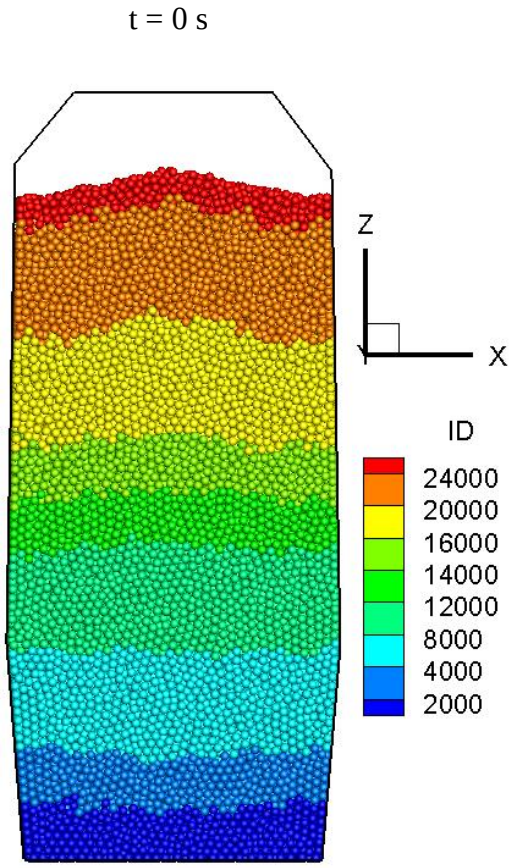

Figure 4.4: Initial state of packed bed: particles colour-coded by index (ID).

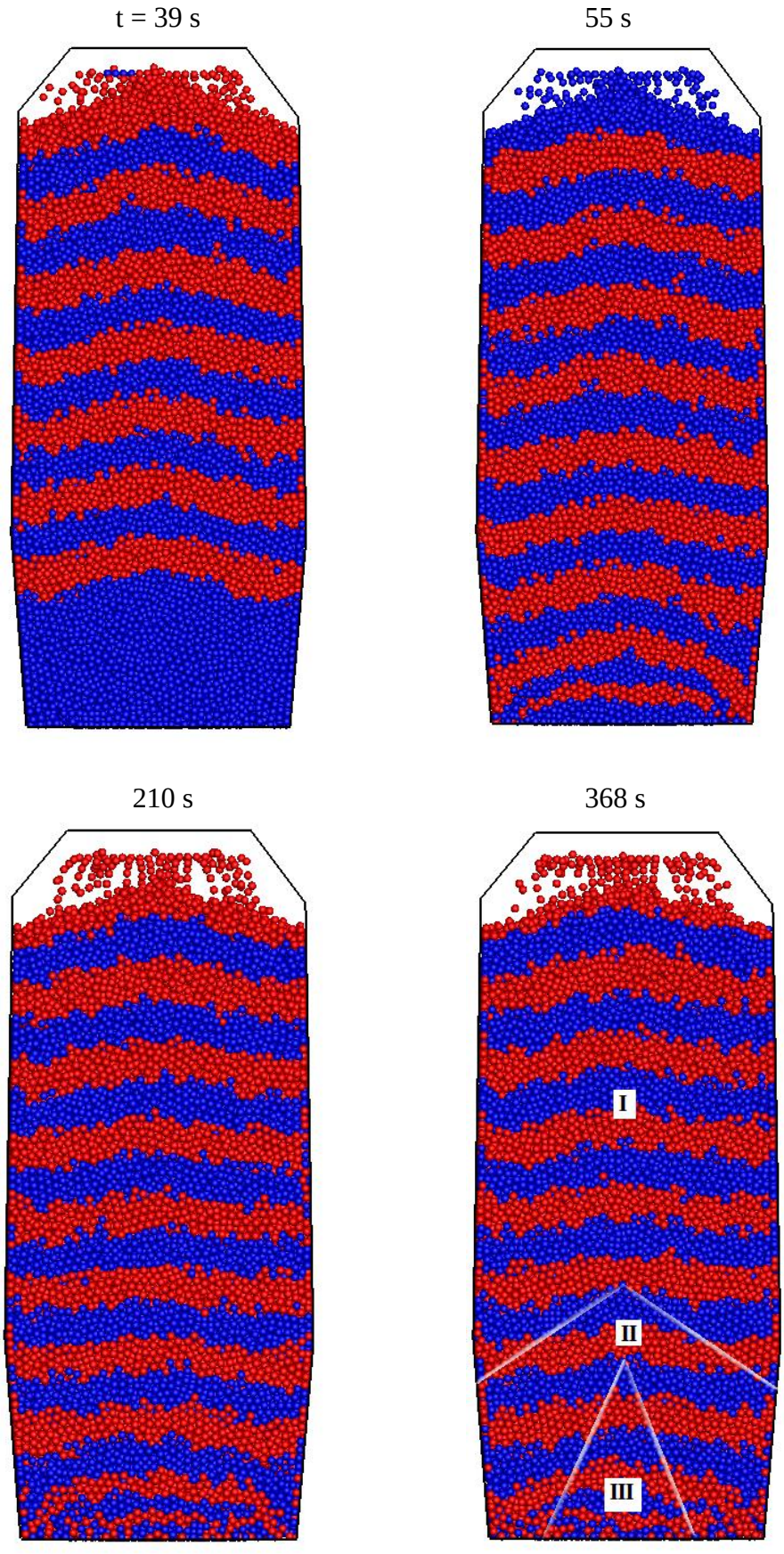

Figure 4.5: Snapshots of solid flow patterns at different times with inlet velocity of 2 m/s.

A relatively uniform charge or burden distribution is adopted, as its effect is not the focus of interest here (this effect will be considered in Chapter 6). As can be seen in Figure 4.5, a relatively stable solid flow is observed at 55 s; after this time, however, some minor changes are observed, with two main features. The first of these is the slow motion of particles near wall, due mainly to particle-wall friction. The second feature is the formation of three different flow zones, such as the plug flow zone at the top (I), the stagnant zone (commonly called the "deadman" in this context) at the lower central part (III), and the quasi-stagnant zone (II), as indicated schematically by the white lines in the snapshot at 368 s (Figure 4.5). In the plug flow zone, particles descend with a relatively uniform velocity across the model. It is worth noting that the quasi-stagnant zone in the COREX RS is similar in location to that in BF (Zhou et al., 2011). The main reason for this phenomenon is that during discharging, particles tend to move under gravitational force into the voids formed at the tips of the screws. The granules are then mechanically transferred from the RS and through the spiral path between the screws' blades. In this way, a quasi-stagnant zone is formed above the screws, ending near the wall. The motion of particles in the stagnant zone is slow by comparison with other zones, mainly because of the complicated flow characteristics and high particle-particle contact forces in this area.

The same analysis was carried out at different inlet gas velocities (4–6 m/s) as shown in Figure 4.6. As can be seen, there is no pronounced difference in all cases, which was to be expected, as the gas velocity inlet has only a minor effect on the moving bed solid flow inside the RS, agreeing well with physical simulation results by H. Zhou et al. (2015).

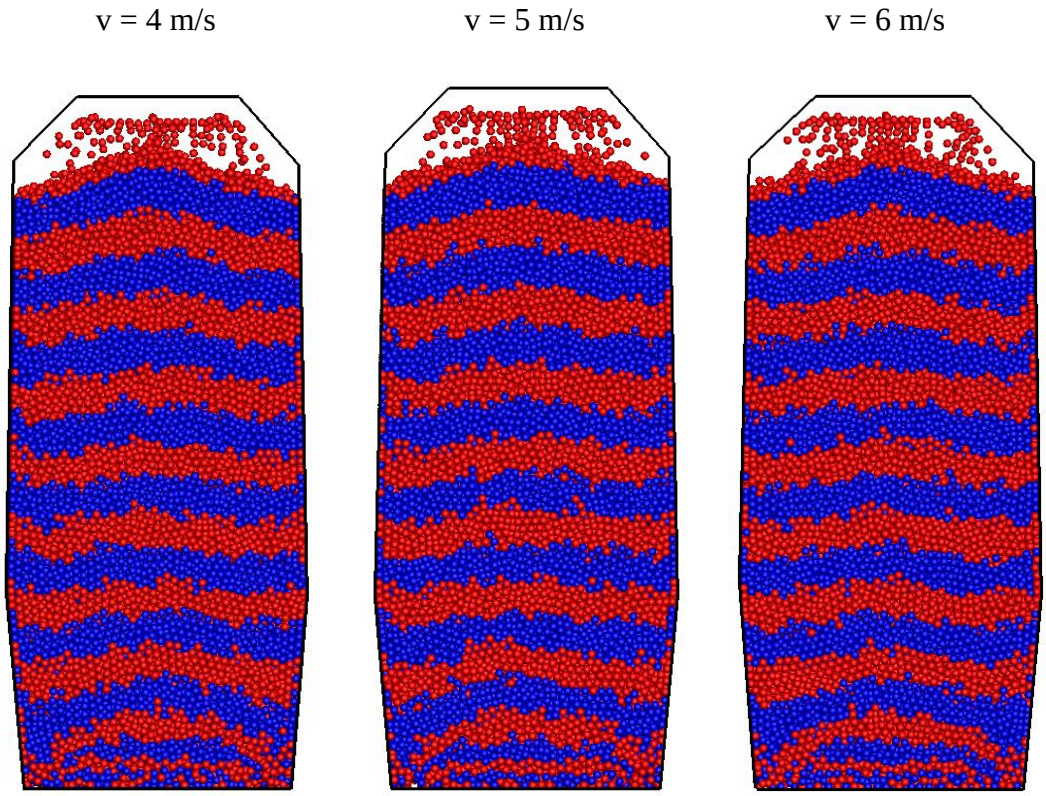

Figure 4.6: Snapshots of solid flow patterns at different inlet gas velocities at 368 s.

Further analyses were conducted in relation to gas flow and porosity distribution. As shown in Figure 4.7, flow fields are almost identical at all inlet gas velocities (2–6 m/s). The areas showing small velocities correspond to the quasi-stagnant and stagnant zones of the solid flow. In the plug flow zone, the gas velocity is fairly uniform, providing a good environment for iron ore reduction, while in the quasi-stagnant zones, the gas velocity fades as it moves across the discharging outlet. No significant difference of porosity distribution is observed, indicating that gas flow has only a minor effect on the gas-solid flow pattern.

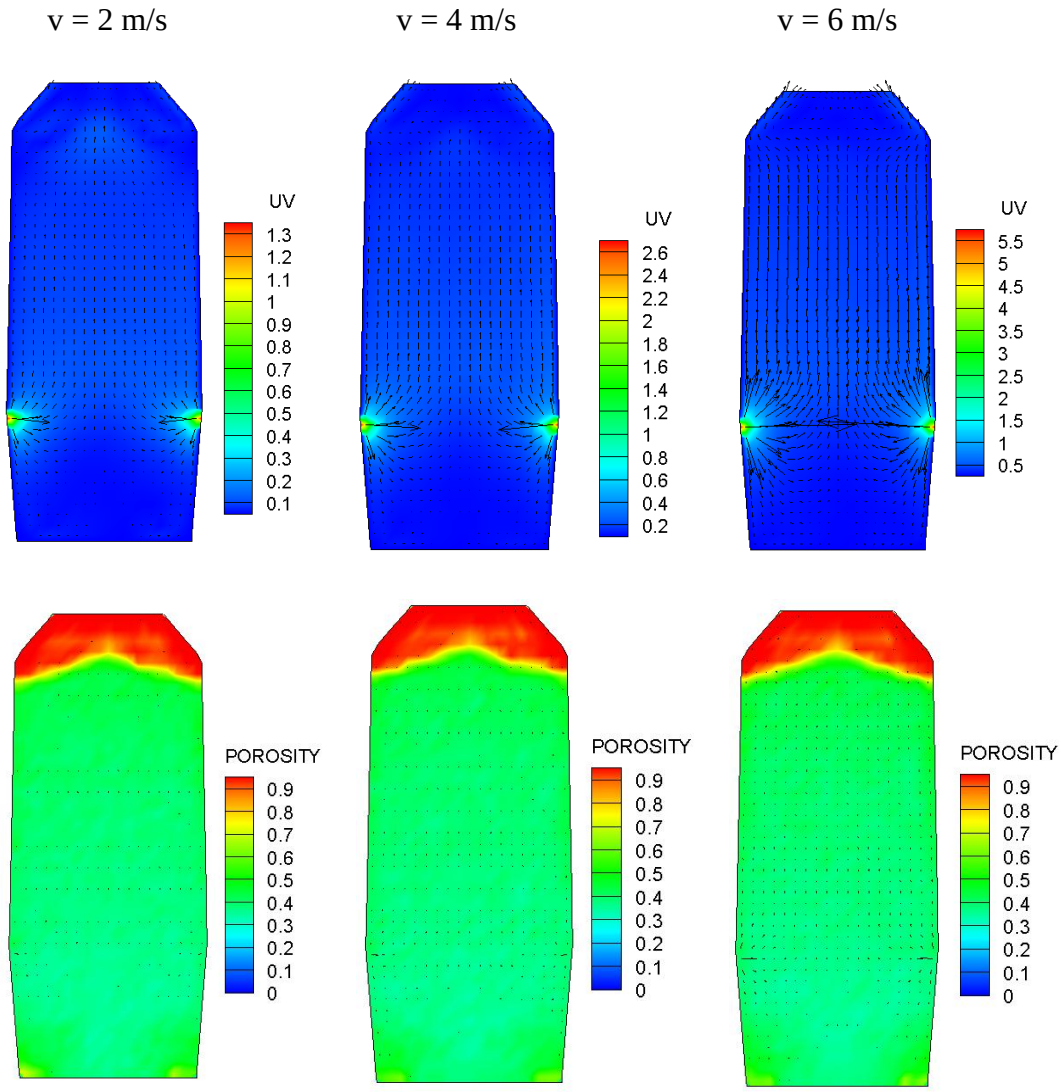

Figure 4.7: Gas flow (top) and porosity distribution (bottom) at different inlet gas velocities.

4.3 Summary

CFD-DEM techniques have been employed here to understand gas-solid flow in the reduction shaft of the COREX process, and to investigate the effect of different gas velocities on solid flow pattern. The results indicate that gas flow has a minimal effect on solid flow pattern due to small gas-solid interaction forces. It follows that solid flow in the reduction shaft can be investigated by examining only the solid phase, if the effects of other factors like chemical reactions and heat transfer are not necessarily considered. In the current model, two main features are observed. The first is the slow

motion of particles near the wall, owing mainly to particle-wall friction. The second feature is the formation of different flow zones, such as the plug flow zone at the top, the stagnant zone at the central-bottom and the quasi-stagnant zone in-between and near the discharging outlet.

Chapter 5 HEAT TRANSFER CHARACTERISTICS IN REDUCTION SHAFT

There are complicated multiphase flow, heat transfer and chemical reactions taking place simultaneously in the COREX RS. It is important to understand heat transfer characteristics, as the thermal-chemical behaviour of particles in interaction with gas could affect the performance of moving bed reactors. The heat produced by reducing gas provides adequate energy for reduction. However, this energy should be optimized so that the iron ore is reduced to a certain degree of metallization without reaching the melting condition of burden materials. A 2D CFD-DEM model is used here with two particle types (iron and coal) as detailed in the next section.

5.1 Simulation Conditions

The geometry used here is the same as that previously used in gas-solid flow cases. However, in the heat transfer study, different properties are chosen for coke and iron ore respectively according to the data in literature. It should be noted that reducing gas is injected at 120 s in the simulation at a temperature of 1000 °C. Details of the particle and gas properties used in the simulation are listed in Table 5.1.

Table 5.1: Particle and gas properties.

Parameters	*Values*
Iron Ore Particles	Diameter = 60 mm
	Density = 4300 kg/m^3
	Initial temperature = 25 °C
	Thermal conductivity = 80 $Wm^{-1}K^{-1}$
	Heat capacity = 6 $Jkg^{-1}K^{-1}$
Coal Particles	Diameter = 40 mm
	Density = 2500 kg/m^3
	Initial temperature = 25 °C
	Thermal conductivity = 1.70 $Wm^{-1}K^{-1}$
	Heat capacity = 8.50 $Jkg^{-1}K^{-1}$
Gas	Density at room temperature = 1.2 kg/m^3
	Viscosity at room temperature = 1.8E^{-5} Pa s
	Inlet temperature = 1000 °C
	Inlet velocity = 10.2 m/s
	Thermal conductivity = 0.0262 $Wm^{-1}K^{-1}$
	Heat capacity = 1000 $Jkg^{-1}K^{-1}$

5.2 Effect of Discharging Flowrate

Figure 5.1 shows the heating process of burden materials in a RS when the inlet gas velocity is 10.2 m/s. The hot reducing gas is assumed to be injected at 1000 °C from both sides of the RS at time 120 s. It should be noted that this gas temperature is slightly higher than the actual temperature of 850 °C in real operation. At the raceway region, particles are heated quickly, and the temperature of all particles increases gradually until they reach a constant temperature (i.e. the gas inlet temperature of 1000 °C). However, this temperature was not reached, as it takes a too long computation time to achieve the thermal equilibrium.

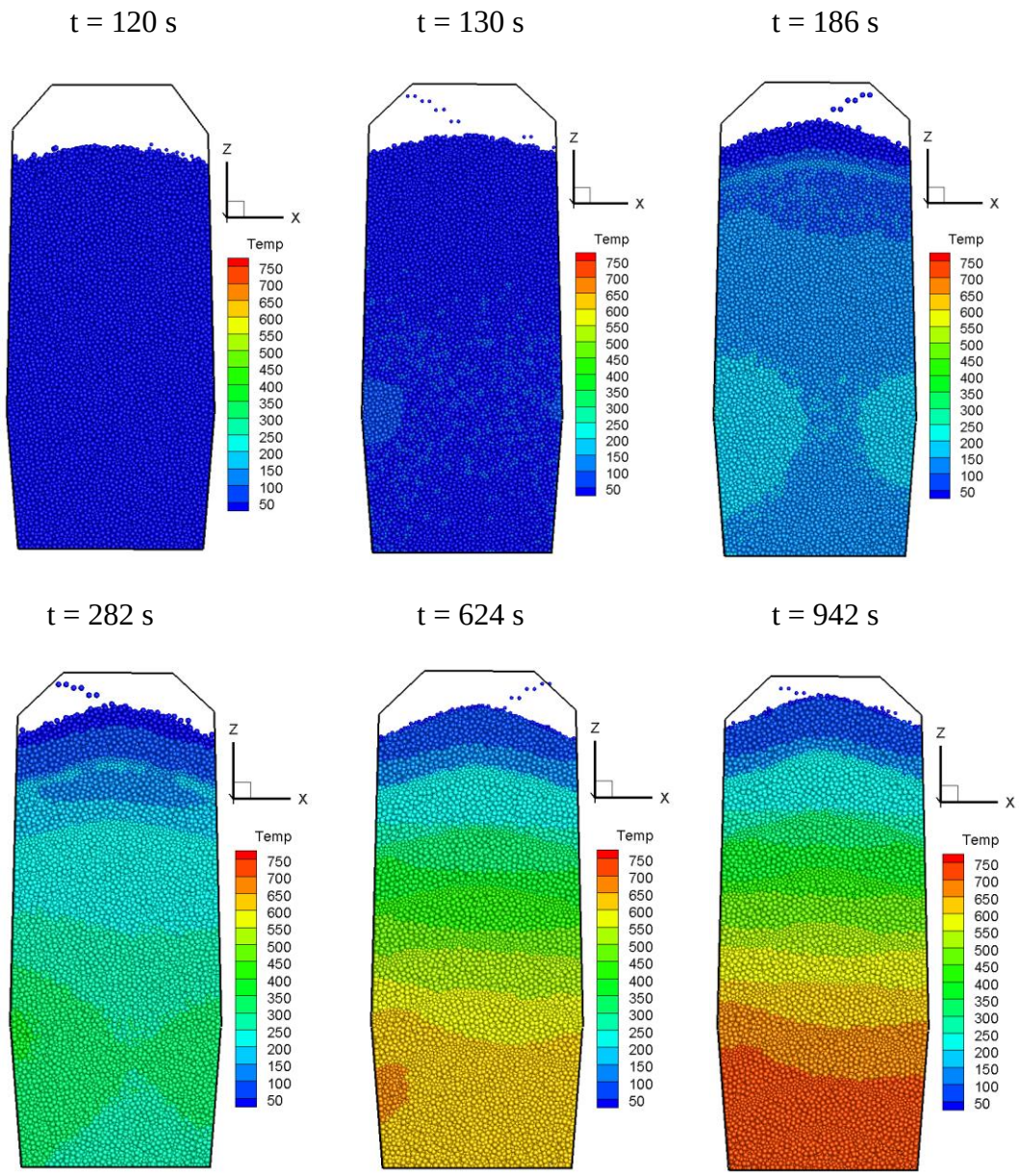

Figure 5.1: Snapshots of solid temperature distribution in the RS at 1000 °C inlet gas temperature and 10.2 m/s gas velocity.

The effect of different discharge flowrates on particles temperature was then investigated. In general, a fast discharging rate is responsible for poor metallization of product materials (DRI). On the other hand, if the discharging rate is slow, particles may reach melting point, which eventually increases the tendency for particles to stick to each other. As shown in Figure 4.2, four different discharging rates were tested here.

The objective was to achieve the thermal equilibrium state within a short period of time (i.e. simulation duration ~ 1000 s).

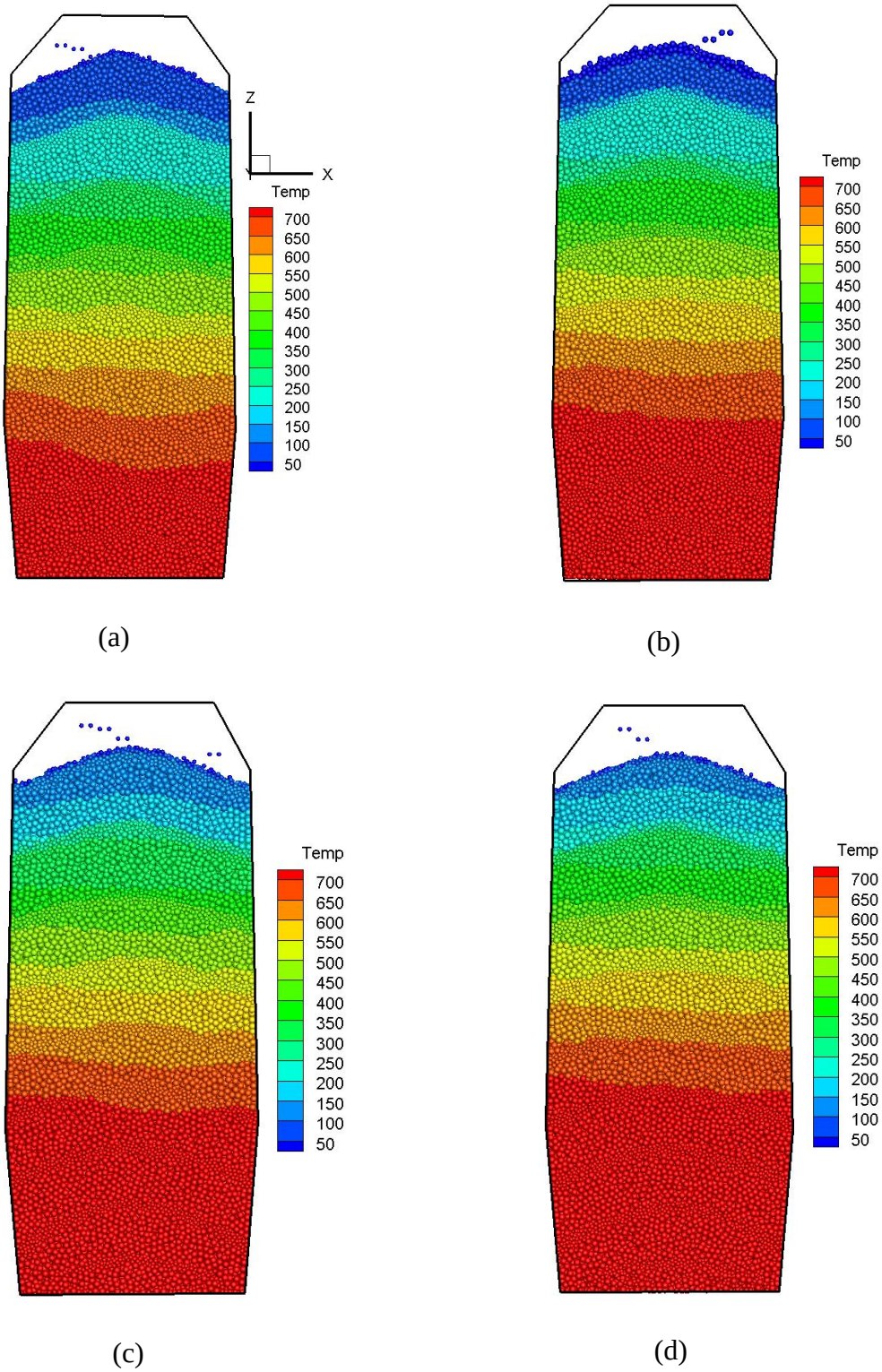

Figure 5.2: Snapshots of solid temperature distribution in the RS at different discharging rates: (a) 18.07 kg/s; (b) 16.07 kg/s; (c) 15.22 kg/s; (d) 13.77 kg/s.

Figure 5.3: Average bed temperature with time at different discharging rates shows how average bed temperature increases as the discharging rate is reduced. Here, 13.77 kg/s (case (d) in Figure 5.2: Snapshots of solid temperature distribution in the RS at different discharging rates: (a) 18.07 kg/s; (b) 16.07 kg/s; (c) 15.22 kg/s; (d) 13.77 kg/s) is favourable for achieving a higher reduction rate and so attaining a better DRI quality. However, the residence time of particles inside the RS must be optimised in order to achieve an optimal level of metallization with the lowest possible process duration and energy, and to avoid sticking of particles. The other obvious feature of the figure is that the heat transfer rate is noticeably higher at the initial stage because of the large temperature gap between gas and particles; the heat transfer rate subsequently slows down when the average bed temperature rises and approaches the gas temperature of the raceway.

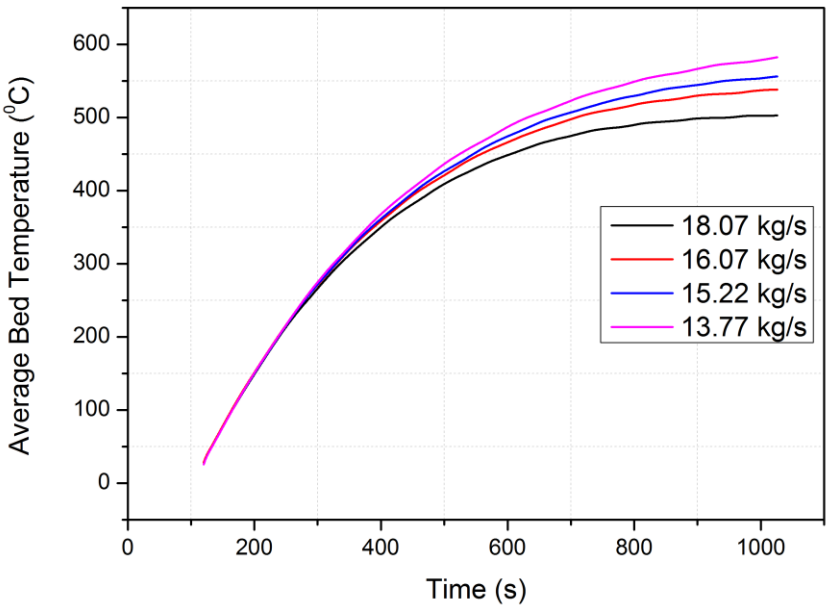

Figure 5.3: Average bed temperature with time at different discharging rates.

Figure 5.4 shows the porosity distribution at time 1000 s, at different discharging rates. Apparently, there are no major differences among all the cases, as the increment of discharging rates is minimal from one case to another.

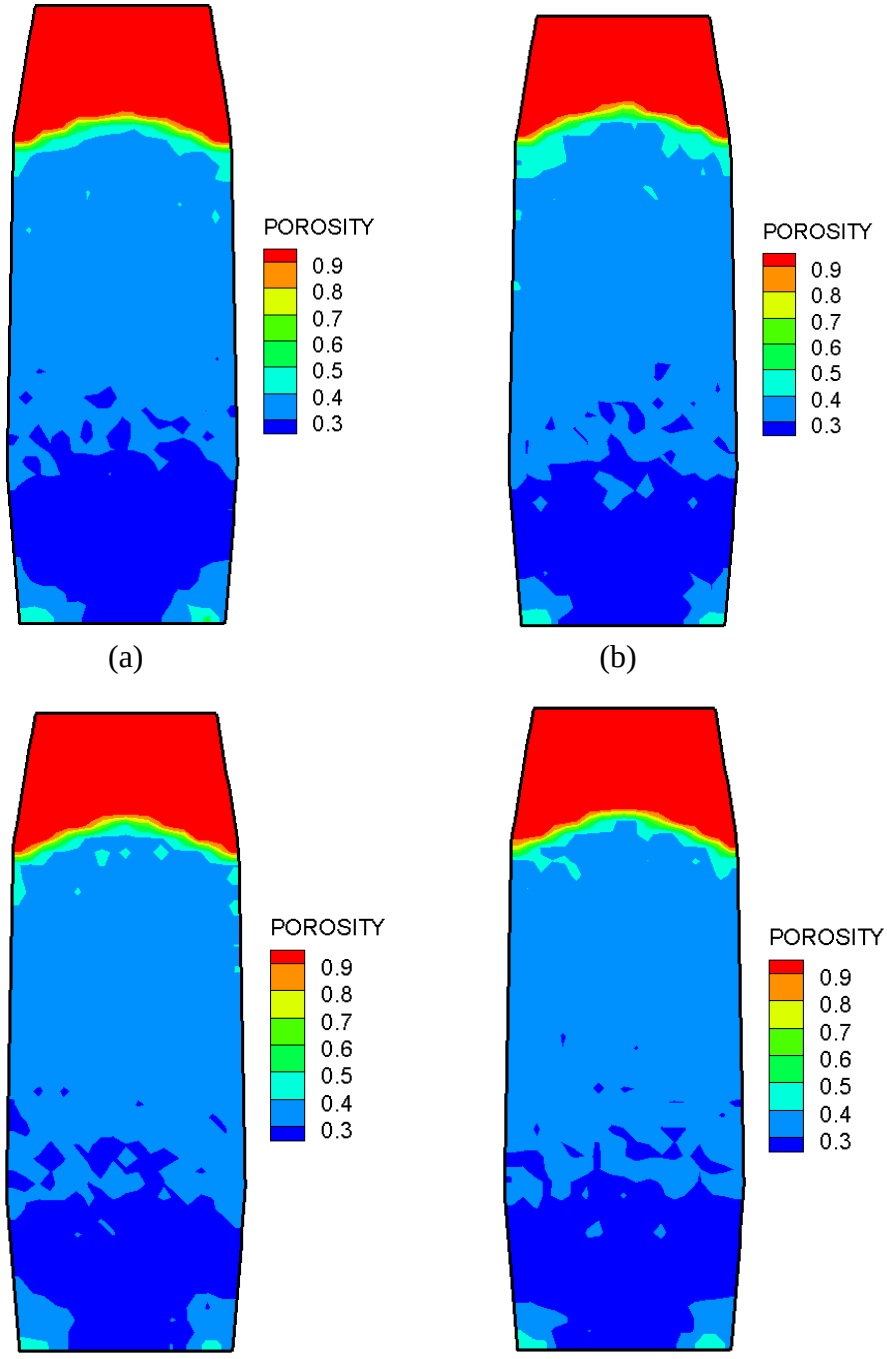

Figure 5.4: Porosity distribution at time 1000 s: (a) 18.07 kg/s; (b) 16.07 kg/s; (c) 15.22 kg/s; (d) 13.77 kg/s.

5.3 Summary

The CFD-DEM approach has been successfully applied to the study of heat transfer in a COREX reduction shaft, and the main features of heat transfer were successfully captured. For instance, it is clear that particles near the bustle zone were heated first and faster than those located further away. Additionally, the heat transfer rate (i.e. the average bed temperature) increased noticeably at the initial stage of the simulation and then barely increased as the average bed temperature reached the inlet gas temperature. However, it should be noted that the simulation needs a very long computational time to reach the thermal equilibrium. Through the development of information technology— for example, using GPU in future studies— computational time can be considerably reduced.

Chapter 6 EFFECT OF BURDEN DISTRIBUTION

Burden distribution has a pronounced effect on heat transfer, gas flow distribution and reduction reactions inside the COREX RS. Moreover, burden distribution can determine gas utilization rate and other economic indices (Xu et al., 2011). While blast furnace burden distribution has received most of the attention (Pandey and Yadav, 1999, Xu et al., 2011), only a few studies have been carried out to investigate effect of burden distribution in the short history of COREX RS (Kou et al., 2013).

This chapter describes a model study conducted with a view to developing a new distribution of burden materials in order to deliver better reduction with low energy consumption. In the regular COREX RS process, the SIMETAL Gimbal Top system charges the iron and coal from the hopper to the furnace. Among its many operational advantages, this charging system can control material distribution effectively by utilizing many chute paths (Whitfield, 2008). The idea here is to charge coal to the central part of furnace, with the iron ore occupying the remaining areas as shown in Figure **6.1**. Supporting concepts for this type of burden distribution include the following.

1. Development of central gas flow: Coal has better permeability due to its high melting point. Reducing gas prefers to travel through areas of minor resistance.
2. Improvement of heat transfer in central region: Coal reactions are exothermic (heat-generating).
3. Improved reduction: Owing to the wall effect, particles near walls usually descend slower than particles in the centre, affording a relatively longer time for particle-gas interactions, and possibly leading to a better reduction.

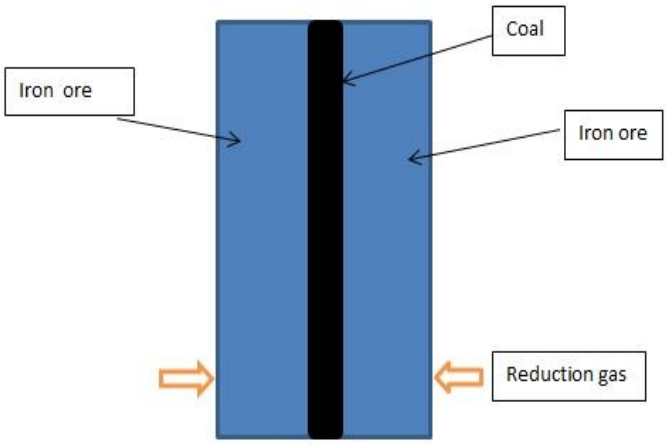

Figure 6.1: New burden arrangement in the RS.

In addition, the reducing gas usually encounters noticeable resistance from the solid flow descending to the bottom of the RS, so that the amount of gas reaching the central part of the RS is not adequate. Increasing the injected gas amount means more energy consumption, which is not desirable. Introduction of the new burden arrangement will encourage more reducing gas to flow through the high permeability areas in the central part of the RS. This arrangement has good potential to improve the gas-coal reaction, leading to heat generation enhancement in this region and in neighbouring areas, and perhaps ultimately to less energy consumption across the whole reduction process.

6.1 Simulation Conditions

Here, a 2-D CFD-DEM slot model is used. The detail of the numerical method for CFD-DEM simulation is set out in section 3.4. The geometry used in this case is the same as that previously used in gas-solid flow cases. Particle and gas properties used in the simulation are detailed in Table **6.1**.

In this model, iron and coal are charged simultaneously from the top of the RS and then allowed to settle. After the settling of particles, the reducing gas is injected from the inlet region with a gas velocity of 10.2 m/s at 120 s.

Table 6.1: Particle and gas properties

Parameters	*Values*
Iron Ore Particles	No. of particles = 10000
	Diameter = 60 mm
	Density = 4300 kg/m^3
	Initial temperature = 25 °C
	Thermal conductivity = 80 $Wm^{-1}K^{-1}$
	Heat capacity = 6 $kg^{-1}K^{-1}$
Coal Particles	No. of particles = 8500
	Diameter = 40 mm
	Density = 2500 kg/m^3
	Initial temperature = 25 °C
	Thermal conductivity = 1.70 $Wm^{-1}K^{-1}$
	Heat capacity = 8.50 $kg^{-1}K^{-1}$
Gas	Density at room temperature = 1.2 kg/m^3
	Viscosity at room temperature = $1.8E^{-5}$ Pa s
	Inlet temperature = 1000 °C
	Inlet velocity = 10.2 m/s
	Thermal conductivity = 0.0262 $Wm^{-1}K^{-1}$
	Heat capacity = 1000 $Jkg^{-1}K^{-1}$

6.2 Effect of Burden Distribution on Bed Temperature

Figure **6.2** shows the new arrangement of burden materials at 291s obtained from the CFD-DEM model. As shown in the figure, coal particles (in red) are charged in the middle region of the RS while ore particles (in blue) are placed so that they surround the coal at the core region. Figure **6.3** shows the effect of the new burden distribution on the average bed temperature at different discharging flowrates. It should be noted that the simulation was terminated in all three cases at a time of 650 s as the average bed temperature becomes constant (Figure **6.4**), requiring extended computation time to reach the thermal equilibrium (i.e. inlet gas temperature). In all the cases, however,

some improvement in heat transfer is observed in the central part of the RS, as shown in Figure **6.3**. Particles in the central region reach a high temperature in the vertical direction faster than those located near the gas inlet region, aligning well with theoretical observations and with the fact that the coal reaction is exothermic. On that basis, coal can be used in the central region to improve gas-solid reactions. However, neither the quantity nor the quality of coal required for optimal operation was investigated here, and such an optimization should be the focus of future studies.

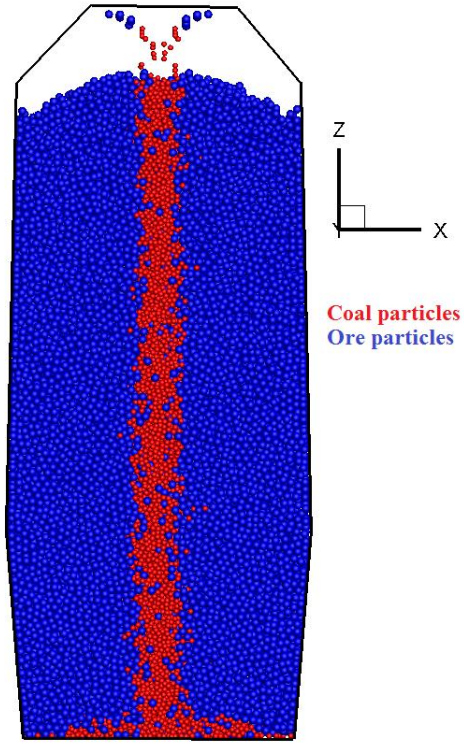

Figure 6.2: New burden distribution at time 291 s in CFD-DEM model.

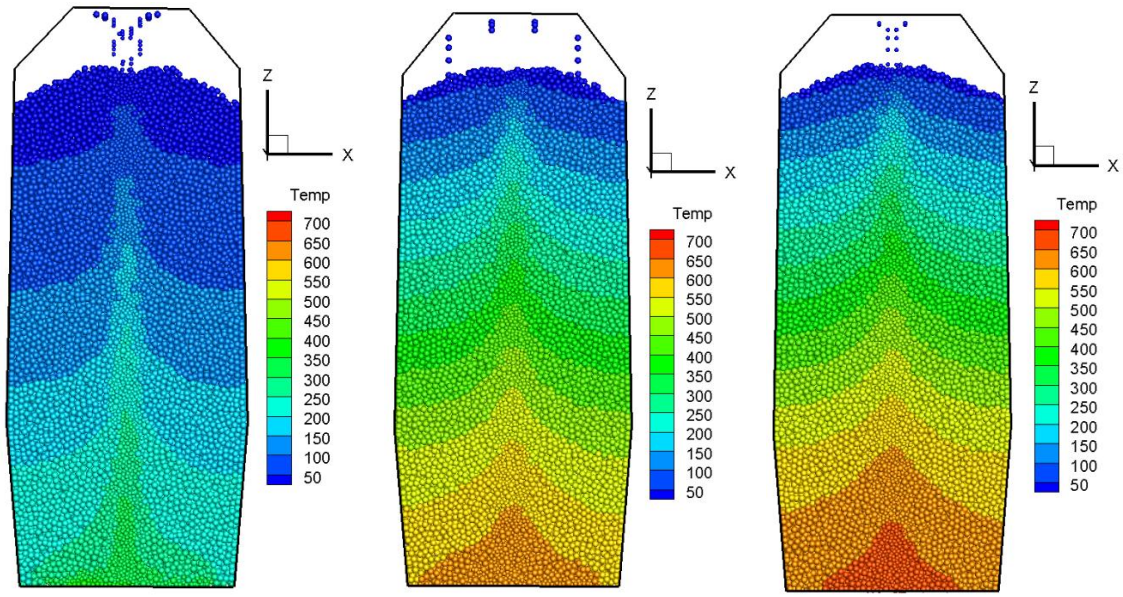

Figure 6.3: Average bed temperature at time 644 s with different particle discharging rates (a) 72.3 kg/s; (b)24.1 kg/s; (c) 20.66 kg/s.

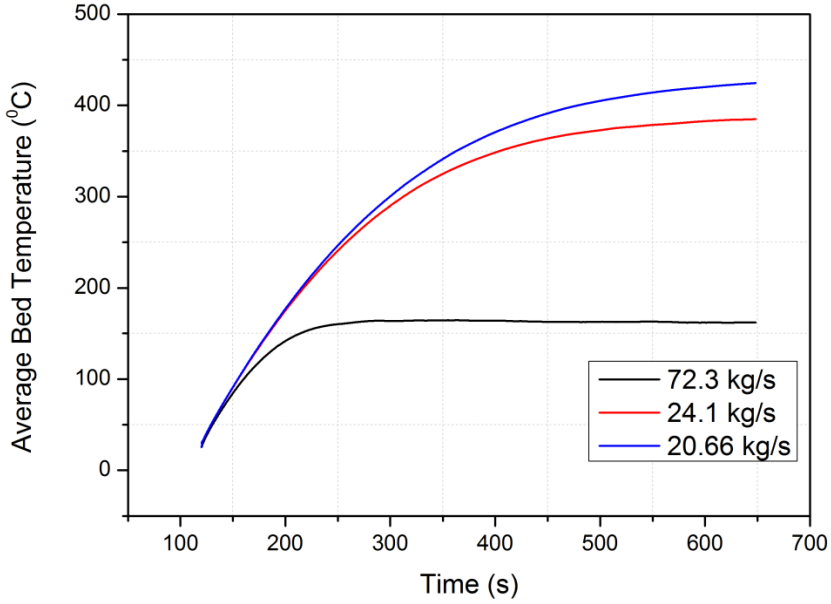

Figure 6.4: Average bed temperature with time at different discharging rates.

6.3 Effect of Burden Distribution on Furnace Porosity

Porosity is a measure of the void spaces in a material, usually defined as the fraction of the volume of the voids over the total volume, with a value between zero and

one. In the RS, maintaining an adequate ratio of porosity is of great importance, as the reducing gas travels through particle voids and voids itself in the burden material, during reduction reactions.

In general, porosity distribution is related to the flow of particles; a high velocity corresponds to a high porosity. Regions of high porosity are associated with the unconfined motion of particles (Zhou et al., 2008b). As shown in Figure **6.5**, the region around the discharging outlet has the highest porosity, and for that reason, particles tend to move into the voids formed at the tips of the screws. Therefore, particles move relatively faster in these regions as compared to other regions inside the RS. By contrast, the motion of particles in the stagnant zone is slow, corresponding to low porosity. In the upper part, corresponding to the plug flow region, porosity does not vary much. It should be noted (as previously elaborated in section 4.2) that inlet gas velocity has only a minimal effect on the porosity distribution inside the RS in all the cases under discussion.

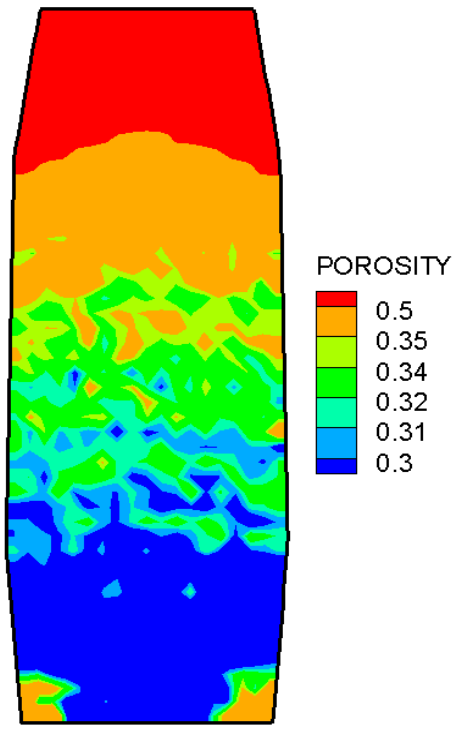

Figure 6.5: Porosity distribution at inlet gas velocity of 10.2 m/s with simplified burden distribution.

Figure **6.6** shows the effect of the proposed burden distribution on porosity ratio at different discharging flowrates. Contrary to expectation, the areas in the central region of the RS are of low porosity and are therefore less permeable for reducing gases. However, this is theoretically understandable, as the coal particles located in the central region are of smaller diameter than the iron ore particles, causing the central area to be more densely stacked (i.e. high coordination number). The undersize coal may disturb the stability of the furnace as it combusts quickly due to its high surface area. Kumar et al. (Kumar et al., 2009) suggests that the mean particle size (MPS) of coal should be kept between 19-22 mm for retaining adequate permeability .This means that, if the furnace contains an extensive amount of fines, the resistance to gas flow will be great so that the RS cannot run effectively. In future studies, more realistic particle properties should be utilized. It is worth noting that a new dense region (i.e. a low porosity area) is generated in the lower middle region of the RS; this can be identified as a new stagnant zone.

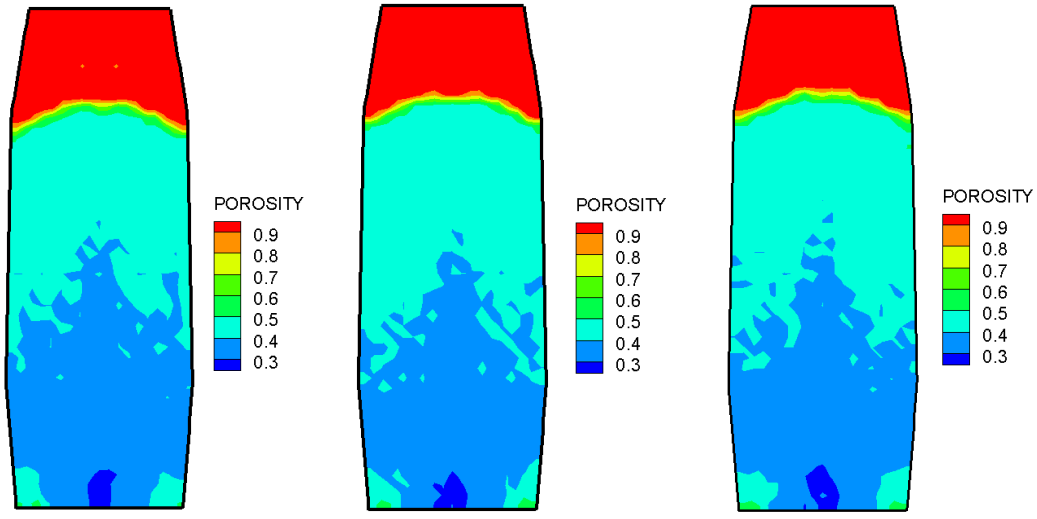

(a) (b) (c)

Figure 6.6: Effect of the new burden distribution on porosity ratio at different discharging flowrates: (a) 72.3 kg/s; (b)24.1 kg/s; (c) 20.66 kg/s.

In order to confirm the effect of coal in promoting average bed temperature, the percentages of heat exchange rate (HER) accounted for by convection, conduction and radiation were examined in both simplified and new burden distributions. As shown in Figure **6.7**, both cases (a) and (b) have similar features for the first 300s of the simulation. After this period, the percentage of convective HER in the new burden distribution (as seen in Figure **6.7**(a)) maintains its share of about 60% of the total HER, which means more efficient gas distribution and therefore better gas-solid reactions. This improvement may be related to CO production from central coal. However, any such argument needs to be supported by further investigation. The percentages of HER by conduction and radiation remained constant in the range of 18-22%, indicating that less heat is transferred through solid-solid contacts. On the other hand, the percentage of HER in normal burden distribution, as shown in Figure **6.7**(b), follows a normal declining curve for convective HER and a rising curve for conduction and radiation HER, until they all reach stable condition after about 800s.

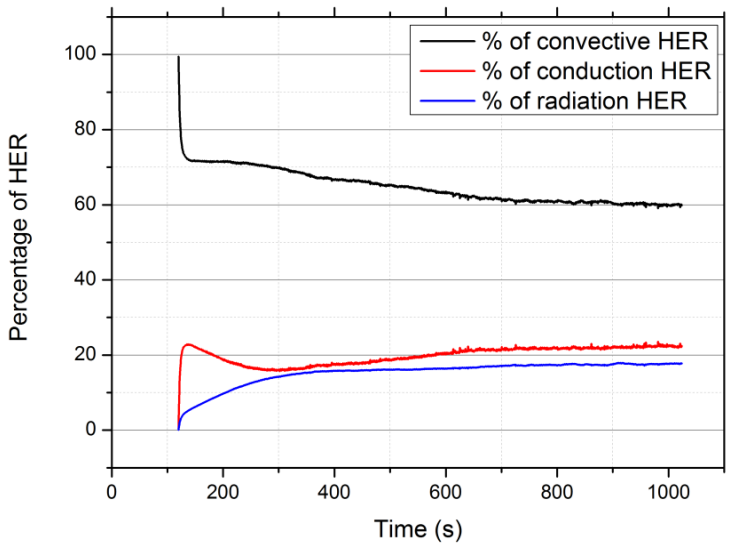

(a)

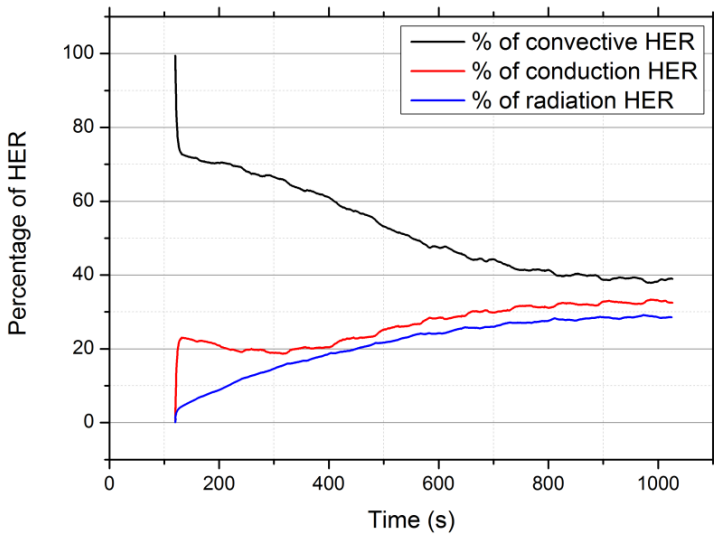

(b)

Figure 6.7: Percentage of heat exchange rate (HER) with time: (a) new burden distribution; (b) simplified burden distribution.

6.4 Summary

A new distribution of burden material has been proposed and investigated by use of the CFD-DEM method. The results show that average bed temperature improved in the

central region of the RS, owing to the increment of convection heat exchange rate (HER) due to coal reactions. The optimum quality and quantity of coal required was not investigated here, and should be included in future studies. The analysis also shows that the porosity ratio in the central region of the reduction shaft decreased because of the smaller size of the coal particles, while the region around the discharging outlet had the highest porosity, owing to fast particle motion in this area. By contrast, the particle motion in the stagnant zone is slow, corresponding to the low porosity. It is suggested that more studies of this kind should be carried out in the future with a view to improving the gas-solid reaction and overall energy consumption.

Chapter 7 SUMMARY AND CONCLUSIONS

A gas-solid and heat transfer model for the COREX reduction shaft was formulated in an attempt to capture the complicated solid characteristics inside the reduction shaft. The effect of sticking phenomena on solid flow inside the reduction shaft was also investigated. The objectives of this project were successfully met by use of CFD-DEM techniques, and the following conclusions can be drawn.

- A two-dimensional slot model was employed to study the effect of gas flow on solid flow patterns. The results indicate that gas flow has a minimal effect on solid flow pattern under the specified conditions, owing mainly to small gas-solid interaction forces. As such, the solid flow inside the reduction shaft can be investigated by considering only the solid phase if the effects of chemical reactions and heat and mass transfer are not necessary to consider.
- Analysis of the CFD-DEM model results reveals two main features inside the reduction shaft. The first is the slow motion of particles near the wall, owing mainly to particle-wall friction. The second feature is the formation of different flow zones such as the plug flow zone at the top, the stagnant zone at the central-bottom, the funnel zone above the tips of the screw dischargers and the quasi-stagnant zone above the screws.
- Heat transfer phenomena in the reduction shaft can be well described by the CFD-DEM model, which includes heat transfer by convection, conduction and radiation. The following features of the heat transfer process were captured. First, particles around bustle regions are heated, and then heat flows upward. Additionally, the heat transfer rate (i.e. at the average bed temperature) increases noticeably at the initial stage of the simulation and then barely increases as the average bed temperature reaches the inlet gas temperature. The average bed temperature varies according to the solid discharging rate.

- A new burden arrangement was proposed, with some improvement in heat transfer between gas and solids. However, further analysis should be conducted with more realistic inputs.

Finally, it is important to note some potential directions for future research. Extensive development of the CFD-DEM model would enable detection of stickiness between particles in in-furnace situations, taking chemical reactions into account. The pronounced effect of the distribution of burden material on the overall process parameters also warrants further study. Further, to cope with the sophisticated characteristics of the gas-solid flow inside the reduction shaft, discharging rates and the design of discharging screws should be further investigated.

REFERENCES

ABDEL, HALIM, K. S., NASR, M. I., EL & GEASSY, A. A. 2011. Developed model for reduction mechanism of iron ore pellets under load. *Ironmaking & Steelmaking,* 38**,** 189-196.

ALAVI SHOUSHTARI, N., HOSSEINI, S. A. & SOLEIMANI, R. 2013. Investigation of segregation of large particles in a pressurized fluidized bed with a high velocity gas: A discrete particle simulation. *Powder Technology,* 246**,** 398-412.

ANAMERIC, B. & KAWATRA, S. K. 2008. DIRECT IRON SMELTING REDUCTION PROCESSES. *Mineral Processing and Extractive Metallurgy Review,* 30**,** 1-51.

ANDERSON, T. B. & JACKSON, R. 1967. Fluid mechanical description of fluidized beds-equations of motion. *Industrial & Engineering Chemistry Fundamentals,* 6**,** 527-539.

ASMAR, B. N., LANGSTON, P. A., MATCHETT, A. J. & WALTERS, J. K. 2002. Validation tests on a distinct element model of vibrating cohesive particle systems. *Computers & Chemical Engineering,* 26**,** 785-802.

BARMAN, S. C., MRUNMAYA, K. P. & RANJAN, M. 2011. Mathematical Model Development of Raceway Parameters and Their Effects on Corex Process. *Journal of Iron and Steel Research, International,* 18**,** 20-24.

BASDAĞ, A. & AROL, A. I. 2002. Coating of iron oxide pellets for direct reduction. *Scandinavian Journal of Metallurgy,* 31**,** 229-233.

BATCHELOR, G. K. & BRIEN, R. W. 1977. Thermal or Electrical Conduction Through a Granular Material. *Proceedings of the Royal Society of London A: Mathematical, Physical and Engineering Sciences,* 355**,** 313-333.

CARAM, H. & HONG, D. C. 1991. Random-walk approach to granular flows. *Physical Review Letters,* 67**,** 828-831.

CHATTERJEE, A. 2005. 'A critical appraisal of the present status of smelting reduction—Part I: From blast furnace to Corex. *Steel Times International***,** 23-31.

CHAUDHURI, B., MEHROTRA, A., MUZZIO, F. J. & TOMASSONE, M. S. 2006. Cohesive effects in powder mixing in a tumbling blender. *Powder Technology,* 165**,** 105-114.

CHENG, G. J., YU, A. B. & ZULLI, P. 1999. Evaluation of effective thermal conductivity from the structure of a packed bed. *Chemical Engineering Science,* 54**,** 4199-4209.

DRAHUN, J. A. & BRIDGWATER, J. 1983. The mechanisms of free surface segregation. *Powder Technology,* 36**,** 39-53.

EL-GEASSY, A. A., NASR, M. I. & HESSIEN, M. M. 1996. Effect of Reducing Gas on the Volume Change during Reduction of Iron Oxide Compacts. *ISIJ International,* 36**,** 640-649.

FENG, Y. Q. & YU, A. B. 2004. Assessment of Model Formulations in the Discrete Particle Simulation of Gas−Solid Flow. *Industrial & Engineering Chemistry Research,* 43**,** 8378-8390.

GERNON, T. M. & GILBERTSON, M. A. 2012. Segregation of particles in a tapered fluidized bed. *Powder Technology,* 231**,** 88-101.

GRANSDEN, J. F. & SHEASBY, J. S. 1974. The sticking of iron ore during reduction by hydrogen in a fluidized bed. *Canadian Metallurgical Quarterly,* 13**,** 649-657.

HAYASHI, S. & IGUCHI, Y. 1992. Factors Affecting the Sticking of Fine Iron Ores during Fluidized Bed Reduction. *ISIJ International,* 32**,** 962-971.

HIGUCHI, K. & HEEREMA, R. H. 2005. Influence of Artificially Induced Porosity on Strength and Reduction Behavior of Hematite Compacts. *ISIJ International,* 45**,** 574-581.

HONG, D. C. & CARAM, H. S. 1992. DIFFUSING VOID MODEL FOR GRANULAR FLOW. *Modern Physics Letters B,* 06**,** 761-771.

HOOMANS, B. P. B., KUIPERS, J. A. M., BRIELS, W. J. & VAN SWAAIJ, W. P. M. 1996. Discrete particle simulation of bubble and slug formation in a two-

dimensional gas-fluidised bed: A hard-sphere approach. *Chemical Engineering Science,* 51**,** 99-118.

HOU, Q.-F., SAMMAN, M., LI, J. & YU, A.-B. 2014. Modeling the Gas-solid Flow in the Reduction Shaft of COREX. *ISIJ International,* 54**,** 1772-1780.

HOU, Q.-F., ZHOU, Z.-Y. & YU, A.-B. 2012a. Computational study of the effects of material properties on heat transfer in gas fluidization. *Industrial & Engineering Chemistry Research,* 51**,** 11572-11586.

HOU, Q. F., ZHOU, Z. Y. & YU, A. B. 2012b. Computational study of heat transfer in a bubbling fluidized bed with a horizontal tube. *AIChE Journal,* 58**,** 1422-1434.

HOU, Q. F., ZHOU, Z. Y. & YU, A. B. 2012c. Micromechanical modeling and analysis of different flow regimes in gas fluidization. *Chemical Engineering Science,* 84**,** 449-468.

HUANG, Z., YI, L. & JIANG, T. 2012. Mechanisms of strength decrease in the initial reduction of iron ore oxide pellets. *Powder Technology,* 221**,** 284-291.

JULLIEN, R. & MEAKIN, P. 1987. Simple Three-Dimensional Models for Ballistic Deposition with Restructuring. *EPL (Europhysics Letters),* 4**,** 1385.

JULLIEN, R. & MEAKIN, P. 2000. Computer simulations of steepest descent ballistic deposition. *Colloids and Surfaces A: Physicochemical and Engineering Aspects,* 165**,** 405-422.

KOU, M., WU, S., DU, K., SHEN, W., SUN, J. & ZHANG, Z. 2013. DEM Simulation of Burden Distribution in the Upper Part of COREX Shaft Furnace. *ISIJ International,* 53**,** 1002-1009.

KOZICKI, J. & TEJCHMAN, J. 2005. Application of a cellular automaton to simulations of granular flow in silos. *Granular Matter,* 7**,** 45-54.

KUMAR, P. P., BARMAN, S. C., REDDY, B. M. & SEKHAR, V. R. 2009. Raw materials for Corex and their influence on furnace performance. *Ironmaking & Steelmaking,* 36**,** 87-90.

MIDREX TECHNOLOGIES, I. 2014. *2013 World Direct Reduction Statistics* [Online]. http://www.midrex.com/assets/user/media/MIDREX_World_DRI_Stats.pdf: Midrex Technologies, Inc.

MIO, H., YAMAMOTO, K., SHIMOSAKA, A., SHIRAKAWA, Y. & HIDAKA, J. 2007. Modeling of Solid Particle Flow in Blast Furnace Considering Actual Operation by Large-scale Discrete Element Method. *ISIJ International,* 47**,** 1745-1752.

ORTIZ, U., AGUILAR, J., BERRÚN, J. & VIRAMONTESB, R. 1999. Development of iron layers on the internal wall of reduction reactors. *Ceramics International,* 25**,** 165-175.

PANDEY, B. D. & YADAV, U. S. 1999. Blast furnace performance as influenced by burden distribution. *Ironmaking & Steelmaking,* 26**,** 187-192.

PAYAM, A. F. & FATHIPOUR, M. 2011. A capillary force model for interactions between two spheres. *Particuology,* 9**,** 381-386.

RAHMAN, M., SHINOHARA, K., ZHU, H. P., YU, A. B. & ZULLI, P. 2011. Size segregation mechanism of binary particle mixture in forming a conical pile. *Chemical Engineering Science,* 66**,** 6089-6098.

REN, B., ZHONG, W., CHEN, Y., CHEN, X., JIN, B., YUAN, Z. & LU, Y. 2012. CFD-DEM simulation of spouting of corn-shaped particles. *Particuology,* 10**,** 562-572.

ROSATO, A., PRINZ, F., STANDBURG, K. J. & SWENDSEN, R. 1986. Monte Carlo simulation of particulate matter segregation. *Powder Technology,* 49**,** 59-69.

ROSATO, A., STRANDBURG, K. J., PRINZ, F. & SWENDSEN, R. H. 1987. Why the Brazil nuts are on top: Size segregation of particulate matter by shaking. *Physical Review Letters,* 58**,** 1038-1040.

SHARMA, T., GUPTA, R. C. & PRAKASH, B. 1990. Effect of gangue content on the swelling behaviour of iron ore pellets. *Minerals Engineering,* 3**,** 509-516.

SIEMENS VAI, M. T. G. 2011. *Simetal Corex technology* [Online]. http://www.industry.siemens.com/datapool/industry/industrysolutions/metals/simetal/en/SIMETAL-Corex-technology-en.pdf.

STANDISH, N. 1985. Studies of size segregation in filling and emptying a hopper. *Powder Technology,* 45**,** 43-56.

STRACK, P. A. C. A. D. L. 1979. A discrete numerical model for granular assemblies. *Gdotechnique,* 29**,** 47-65.

SUN, J. & CHEN, M. M. 1988. A theoretical analysis of heat transfer due to particle impact. *International Journal of Heat and Mass Transfer,* 31**,** 969-975.

SUN, J. J., ZHOU, H., LUO, Z. G. & ZOU, Z. S. 2013. Numerical simulation of COREX raceway by coupling between CFD and DEM. *Dongbei Daxue Xuebao/Journal of Northeastern University,* 34**,** 824-827+844.

TSUJI, Y., KAWAGUCHI, T. & TANAKA, T. 1993. Discrete particle simulation of two-dimensional fluidized bed. *Powder Technology,* 77**,** 79-87.

VAYENAS, C. G. 1992. Heterogeneous catalysis in industrial practice, second edition. *Journal of Catalysis,* 134**,** 755.

WALL, D., KEPPLINGER, W. & MILLNER, R. 2011. Smelting-Reduction Export Gas as Syngas in the Chemical Industry. *Steel Research International,* 82**,** 926-933.

WANG, H. & SOHN, H. Y. 2012. Effects of Reducing Gas on Swelling and Iron Whisker Formation during the Reduction of Iron Oxide Compact. *steel research international,* 83**,** 903-909.

WANG, H. T. & SOHN, H. Y. 2011. Effect of CaO and SiO2 on swelling and iron whisker formation during reduction of iron oxide compact. *Ironmaking & Steelmaking,* 38**,** 447-452.

WANG, Z. C., CHU, M. S., LIU, Z. G., CHEN, S. Y. & XUE, X. X. 2012. Effects of Temperature and Atmosphere on Pellets Reduction Swelling Index. *Journal of Iron and Steel Research International,* 19**,** 7-12.

WHITFIELD, P. 2008. Operation and Key Design Features of the SIMETALCIS Gimbal Top. *Rev. Met. Paris,* 105**,** 296-303.

WILLIAMS, J. C. 1976. The segregation of particulate materials. A review. *Powder Technology,* 15**,** 245-251.

WINGROVE, G. 1999. Developments in Ironmaking and Opportunities for Power Generation. *1999 Gasification Technologies Conference*.

XU, B. H. & YU, A. B. 1997. Numerical simulation of the gas-solid flow in a fluidized bed by combining discrete particle method with computational fluid dynamics. *Chemical Engineering Science,* 52**,** 2785-2809.

XU, B. H., YU, A. B., CHEW, S. J. & ZULLI, P. 2000. Numerical simulation of the gas–solid flow in a bed with lateral gas blasting. *Powder Technology,* 109**,** 13-26.

XU, J., WU, S., KOU, M., ZHANG, L. & YU, X. 2011. Circumferential burden distribution behaviors at bell-less top blast furnace with parallel type hoppers. *Applied Mathematical Modelling,* 35**,** 1439-1455.

YI, L., HUANG, Z. & JIANG, T. 2013. Sticking of iron ore pellets during reduction with hydrogen and carbon monoxide mixtures: Behavior and mechanism. *Powder Technology,* 235**,** 1001-1007.

YU, A. B. 2004. Discrete element method: An effective way for particle scale research of particulate matter. *Engineering Computations (Swansea, Wales),* 21**,** 205-214.

YU, A. B. & XU, B. H. 2003. Particle-scale modelling of gas–solid flow in fluidisation. *Journal of Chemical Technology & Biotechnology,* 78**,** 111-121.

ZHANG, B., GONG, X., WANG, Z. & GUO, Z. 2011. Relation between Sticking and Metallic Iron Precipitation on the Surface of Fe2O3 Particles Reduced by CO in the Fluidized Bed. *ISIJ International,* 51**,** 1403-1409.

ZHANG, B., WANG, Z., GONG, X. & GUO, Z. 2012. A comparative study of influence of fluidized conditions on sticking time during reduction of Fe2O3 particles with CO. *Powder Technology,* 225**,** 1-6.

ZHAO, J. & SHAN, T. 2013. Coupled CFD–DEM simulation of fluid–particle interaction in geomechanics. *Powder Technology,* 239**,** 248-258.

ZHOU, H., ZOU, Z. S., LUO, Z. G., ZHANG, T., YOU, Y. & LI, H. F. 2015. Analyses of solid flow in latest design COREX shaft furnace by physical simulation. *Ironmaking & Steelmaking,* 42**,** 209-216.

ZHOU, J. H., YU, A. B. & HORIO, M. 2008a. Finite element modeling of the transient heat conduction between colliding particles. *Chemical Engineering Journal,* 139**,** 510-516.

ZHOU, Z. Y., KUANG, S. B., CHU, K. W. & YU, A. B. 2010. Discrete particle simulation of particle–fluid flow: model formulations and their applicability. *Journal of Fluid Mechanics,* 661**,** 482-510.

ZHOU, Z. Y., YU, A. B. & ZULLI, P. 2009. Particle scale study of heat transfer in packed and bubbling fluidized beds. *AIChE Journal,* 55**,** 868-884.

ZHOU, Z. Y., ZHU, H. P., WRIGHT, B., YU, A. B. & ZULLI, P. 2011. Gas–solid flow in an ironmaking blast furnace-II: Discrete particle simulation. *Powder Technology,* 208**,** 72-85.

ZHOU, Z. Y., ZHU, H. P., YU, A. B., WRIGHT, B. & ZULLI, P. 2008b. Discrete particle simulation of gas–solid flow in a blast furnace. *Computers & Chemical Engineering,* 32**,** 1760-1772.

ZHU, H. P., ZHOU, Z. Y., YANG, R. Y. & YU, A. B. 2007. Discrete particle simulation of particulate systems: Theoretical developments. *Chemical Engineering Science,* 62**,** 3378-3396.